Genetic Background Dominates Fibrotic Aortic Remodeling During Angiotensin-Induced Hypertension in Mice

Bart Spronck[1,2], Alexander W. Caulk[1], Abhay B. Ramachandra[1], Sae-Il Murtada[1], Alexia Rojas[1], Chang-Shun He[1], Matthew R. Bersi[3], George Tellides[4,5], Jay D. Humphrey[1,5]

[1]Department of Biomedical Engineering
Yale University, New Haven, CT, USA

[2]Department of Biomedical Engineering
Maastricht University, Maastricht, Netherlands

[3]Department of Biomedical Engineering
Vanderbilt University, Nashville, TN, USA

[4]Department of Surgery and [5]Vascular
Biology and Therapeutics Program
Yale School of Medicine, New Haven, CT, USA

Running title: Genetic Background in Fibrotic Aortic Remodeling

Keywords: mouse, aorta, strain, stiffness

Address for Correspondence:

J.D. Humphrey, Ph.D.
Department of Biomedical Engineering
Yale University
55 Prospect Street
New Haven, CT 06520 USA
+1-203-432-6428
jay.humphrey@yale.edu

Abstract

Objective. Many genetically-induced mutations affect aortic structure and function in mice, but little is known about the influence of background strain. This study quantifies the aortic phenotype in angiotensin II (AngII)-induced hypertension across different strains of wild-type mice.

Approach and Results. Adult male C57BL/6J and 129SvEv mice were studied before and after induction of hypertension via subcutaneous infusion of AngII (1000 ng/kg/min) for two weeks, which elevated blood pressure similarly (+31% vs. +32%, systolic). The descending thoracic aortas were placed within a custom computer-controlled biomechanical testing device and subjected to a series of isobaric vasocontraction and vasorelaxation tests as well as novel stiffness testing. Immuno-histological studies quantified medial and adventitial composition as well as $CD45^+$ cellular infiltration. Baseline aortic geometry and biomechanical properties were similar across strains, consistent with the existence of general homeostatic mechanical targets. Nevertheless, aortic remodeling due to AngII-induced hypertension differed dramatically between strains, with gross over-adaptive remodeling (exuberant thickening of the media and adventitia) in C57BL/6J but under-adaptive remodeling in 129SvEv mice. Importantly, vasoconstrictive strength was lower in C57BL/6J than 129SvEv mice, both before and after hypertension, while $CD45^+$ cell content was markedly higher in C57BL/6J than 129SvEv mice following hypertension.

Conclusions. Genetic modifiers likely play a key role in the different hypertensive aortic remodeling between C57BL/6J and 129SvEv mice as well as mixed C57BL/6;129SvEv mice. The lower fibrotic response in 129SvEv mice results from their lower inflammatory state but also greater aortic vasoresponsiveness to AngII, which lowers the wall-stress mechano-stimulus for remodeling. Remodeling in mixed background mice is dominated by the 129SvEv strain.

Graphical Abstract

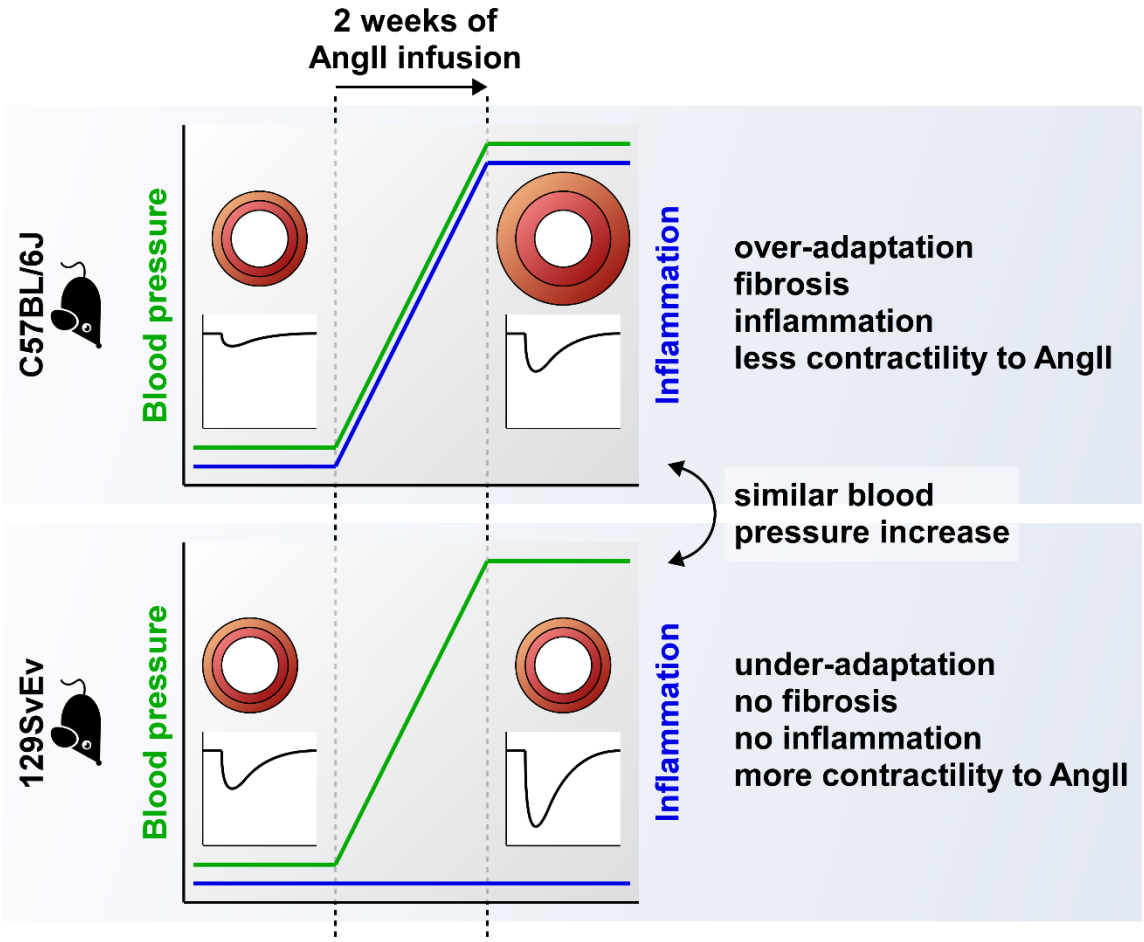

Legend

AngII, angiotensin II;  , *in vitro* contraction to AngII

Abbreviations

a	deformed inner radius
ACh	acetylcholine
AngII	angiotensin II
γ	fold increase in pressure
C	contractile state
CD45	cluster of differentiation 45
DTA	descending thoracic aorta
ε	fold increase in blood flow
Fbln5	fibulin-5
h	deformed wall thickness
HT	hypertensive
L-NAME	N_ω-nitro-L-arginine methyl ester
λ_z	in vivo axial stretch
Mov	Movat's pentachrome
Myh11	smooth muscle myosin heavy chain
NT	normotensive
P	pressure
PE	phenylephrine
σ_θ	circumferential Cauchy stress
$C_{\theta\theta}$	circumferential material stiffness
VVG	Verhoeff–Van Gieson
W	stored energy density
ϕ^e	elastin cross-sectional area fraction
ϕ^c	collagen cross-sectional area fraction
ϕ^m	smooth muscle cross-sectional area fraction
ϕ^g	ground substance/glycosaminoglycan cross-sectional area fraction

Introduction

Mice have emerged as the most common animal model in modern vascular research for many reasons, including the availability of myriad antibodies for biological assays, ease of genetic manipulation, and short gestational period. Consequently, countless models are now available for phenotyping, many of which exist on different backgrounds, including pure and mixed. Pure backgrounds can reduce biological variability and thereby enable meaningful statistical comparisons using smaller numbers of animals. In contrast, mixed backgrounds can exhibit more variability as is common in natural populations, which will be increasingly relevant as we move toward precision medicine. The importance of genetic background is underscored by the current lack of inclusion of diverse ancestral populations in human genomics research (Cornel and Bonham, 2017). Hence, the availability of diverse mouse models on different backgrounds promises to provide important data, though posing a challenge to analysis and interpretation. There is, therefore, a pressing need for comparative studies that provide baseline information.

In many cases, a vascular phenotype is described in clinical terms, including aneurysmal, atherosclerotic, stenotic, and tortuous. We have suggested that there is also a need to phenotype vessels biomechanically (Ferruzzi et al., 2015), given that biomechanics governs many local cellular responses via the (patho)mechanobiology as well as many global circulatory responses via the (patho)physiology (Haga et al., 2007; Davies, 2009; Laurent and Boutouyrie, 2015). Convenient and important metrics for biomechanical phenotyping of the aorta include descriptions of multiaxial wall stress and intrinsic stiffness, the ability to store energy elastically, and the ability to vasoconstrict or vasodilate in response to different stimuli under biaxial loading conditions. We have previously reported biomechanical differences in these metrics as a function of sex and regional location within the central arterial system (Ferruzzi et al., 2015; Bersi et al., 2017; Spronck et al., 2019). Herein, however, we focus on the biomechanical phenotype in males, for which there are more data available for comparison, and one region, the descending thoracic aorta (DTA), which has a propensity for adverse remodeling in hypertension. Moreover, we have previously reported differences as a function of various genetic mutations (e.g., Bellini et al., 2017a; Humphrey and Tellides, 2019). Herein, however,

we focus on intrinsic differences due to the background strain, which has not been studied in detail for the aorta. Specifically, we compare the biomechanical phenotype of three different common strains of "wild-type" mice arising in response to hypertension induced by a chronic infusion of angiotensin II (AngII) over a two-week period. These strains are "pure" C57BL/6J and 129SvEv mice as well as two cohorts of mixed C57BL/6;129SvEv mice, which are often used in studies of the effects of particular genetic mutations.

Material and Methods

Animals. Adult male C57BL/6J mice were obtained from Jackson Laboratories and adult male 129SvEv mice were obtained from Taconic Biosciences. Blood pressure was measured using a standard tail-cuff method (CODA, Kent Scientific, Torrington, CT, USA) while the mice were restrained within a transparent cylindrical tube without medication. Pressures were measured before and after infusion of angiotensin II (AngII; Sigma-Aldrich, St. Louis, MO, USA) at 1000 ng/kg/min for two weeks using an osmotic mini-pump (Alzet model #2004, DURECT Corporation, Cupertino, CA, USA) that was implanted subcutaneously on the flank while the mice were anesthetized with isoflurane (3% for induction, 1.5% for maintenance). Buprenorphine (0.1 mg/kg subcutaneously) was given pre- and post-operatively for analgesia. At the intended endpoint, the mice were euthanized with an intraperitoneal injection of pentobarbital sodium and phenytoin sodium (Beuthanasia-D; 150 mg/kg) and the DTA was harvested. All data collection and analysis was completed for n = 6–8 mice for each of the four primary study groups: normotensive (NT) and hypertensive (HT) C57BL/6J and 129SvEv mice. All animal protocols were approved by the Yale University Institutional Animal Care and Use Committee and conformed to the current National Institutes of Health guidelines.

In addition, to broaden the range of our comparisons, we also include historical passive data from our laboratory for mixed background C57BL/6;129SvEV mice from two studies of genetic mutations, one for fibulin-5 ($Fbln5^{-/-}$) and one for smooth muscle myosin heavy chain ($Myh11^{R247C/R247C}$). Specifically, the experimental testing protocols and data analysis were identical for the following two mixed background strains: C57BL/6;129SvEv$_{Fbln5}$, which were obtained by breeding $Fbln5^{+/-}$ mice and selecting the $Fbln5^{+/+}$ mice, and C57BL/6;129SvEv$_{Myh11}$,

which were obtained by breeding *Myh11*$^{+/R247C}$ mice and selecting the *Myh11*$^{+/+}$ mice. Further details on these mice and their phenotypes can be found elsewhere (Ferruzzi et al., 2015; Bellini et al., 2015).

Biomechanical Testing. Excised vessels were mounted on custom drawn glass cannulae and secured at each end with 6-0 silk sutures. They were then placed within a custom computer-controlled biaxial device for biomechanical testing (Gleason et al., 2004) and immersed in a heated (37°C) and oxygenated (95%/5% O_2/CO_2) Krebs-Ringer bicarbonate buffered solution containing 2.5 mM $CaCl_2$. The vessels were then subjected to a series of isobaric (luminal pressure of 90 mmHg) - axially isometric (fixed in vivo axial stretch) protocols wherein the vessels were contracted with 100 mM KCl, relaxed (KCl washed out), contracted with 1 μM AngII, relaxed (AngII washed out), contracted with 1 μM phenylephrine (PE), then dilated with 10 μM acetylcholine (ACh; without wash-out), an endothelial cell dependent stimulant of nitric oxide synthesis, and finally exposed to 1 mM N_ω-Nitro-L-arginine methyl ester (L-NAME), a blocker of endogenous production of nitric oxide (a potent vasodilator).

Once these contraction-relaxation protocols were completed, the normal Krebs solution was washed out and replaced with a Ca^{2+}-free Krebs solution to ensure a sustained passive behavior while maintaining heating and oxygenation. Vessels were then preconditioned via four cycles of pressurization between 10 and 140 mmHg while held fixed at their individual in vivo axial stretch. Finally, specimens were exposed to three pressure-diameter (*P-d*) protocols, with luminal pressure cycled between 10 and 140 mmHg while axial stretch was maintained fixed at either the in vivo value or ±5% of this value, and to four axial force-length (*f-l*) tests, with force cycled between 0 and a force equal to the maximum value measured during the pressurization test at 5% above the in vivo axial stretch value, while the luminal pressure was maintained fixed at 10, 60, 100, or 140 mmHg. Pressure, axial force, outer diameter, and axial length were recorded on-line for all seven of these protocols and used for subsequent data analysis.

Passive Descriptors. We have found that five key biomechanical metrics define well the passive mechanical phenotype of the aorta: mean circumferential and axial wall stress, circumferential and axial material stiffness, and the elastically stored energy. Each of these metrics is calculated easily given best-fit values of the model parameters within a nonlinear

stored energy function, which herein is assumed consistent with prior studies (Ferruzzi et al., 2015; Bellini et al., 2015, 2017a; Bersi et al., 2016, 2017), namely

$$W\left(\mathbf{C},\mathbf{M}^{j}\right)=\frac{c}{2}\left(I_{\mathbf{C}}-3\right)+\sum_{j=1}^{4}\frac{c_{1}^{j}}{4c_{2}^{j}}\left\{\exp\left[c_{2}^{j}\left(IV_{\mathbf{C}}^{j}-1\right)^{2}\right]-1\right\}, \tag{1}$$

where c, c_1^j, and c_2^j ($j=1,2,3,4$) are model parameters. $I_{\mathbf{C}}=\mathbf{C}:\mathbf{I}$ and $IV_{\mathbf{C}}^{j}=\mathbf{C}:\mathbf{M}^{j}\otimes\mathbf{M}^{j}$ are coordinate invariant measures of deformation, with $\mathbf{I}$ the identity tensor and $\mathbf{C}=\mathbf{F}^{\mathrm{T}}\mathbf{F}$ the right Cauchy-Green tensor, with $\mathbf{F}$ the deformation gradient tensor and the superscript T a transpose; $\det\mathbf{F}=1$ because of assumed incompressibility. The direction of the j^{th} family of fibers is given by the unit vector $\mathbf{M}^{j}=\left[0,\ \sin\alpha_{0}^{j},\ \cos\alpha_{0}^{j}\right]$, with angle α_0^j computed with respect to the axial direction in a reference configuration. Based on prior microstructural observations, and the yet unknown effects of cross-links and physical entanglements amongst the multiple families of fibers, we included contributions of axial ($\alpha_0^1=0$), circumferential ($\alpha_0^2=\pi/2$), and two symmetric diagonal families of fibers ($\alpha_0^{3,4}=\pm\alpha_0$) to capture phenomenologically the complex biaxial behavior; this relation has been validated independently (Schroeder et al., 2018). The Cauchy stress tensor $\mathbf{t}$ is thus

$$\mathbf{t}=-p\mathbf{I}+2\mathbf{F}\frac{\partial W}{\partial\mathbf{C}}\mathbf{F}^{\mathrm{T}}, \tag{2}$$

where p is a Lagrange multiplier that enforces incompressibility. Theoretical values of the applied loads were computed from components of Cauchy stress by solving global equilibrium equations in the radial and axial directions. Best-fit values of the eight model parameters were estimated via nonlinear regression to minimize the sum-of-the-squared differences between experimentally-measured and theoretically-predicted values of luminal pressure and axial force, each normalized by average experimental measures (Ferruzzi et al., 2015). Estimated parameters (constrained to be non-negative) were used to compute stress, material stiffness, and stored energy at any configuration. For example, components of the stiffness tensor ($\mathscr{C}_{ijkl}$), linearized about a configuration defined by the systolic pressure and in vivo axial stretch, were computed as

$$\mathscr{C}_{ijkl} = 2\delta_{ik}F^o_{lA}F^o_{jB}\frac{\partial W}{\partial C_{AB}} + 2\delta_{jk}F^o_{iA}F^o_{lB}\frac{\partial W}{\partial C_{AB}} + 4F^o_{iA}F^o_{jB}F^o_{kP}F^o_{lQ}\frac{\partial^2 W}{\partial C_{AB}\partial C_{PQ}}\bigg|_{\mathbf{C}^o}, \tag{3}$$

where δ_{ij} are components of $\mathbf{I}$, $\mathbf{F}^o$ is the deformation gradient tensor between the chosen reference configuration and a finitely deformed in vivo configuration, and $\mathbf{C}^o$ is the corresponding right Cauchy-Green tensor.

Local Mechano-Adaptations. Copious studies suggest that arteries tend to mechano-adapt in response to modest changes in blood flow and blood pressure, that is, to maintain the flow-induced mean wall shear stress and pressure-induced mean circumferential wall stress near homeostatic targets (Dajnowiec and Langille, 2007; Humphrey, 2008; Hayashi and Naiki, 2009). If we let ε denote the fold increase in blood flow ($\varepsilon = Q/Q_{\mathrm{h}}$) and γ the fold increase in blood pressure ($\gamma = P/P_{\mathrm{h}}$), then it can be shown that a local mechano-adaptive response is given by $a \rightarrow \varepsilon^{1/3}a_{\mathrm{h}}$ and $h \rightarrow \varepsilon^{1/3}\gamma h_{\mathrm{h}}$, where a is the current luminal radius and h the current wall thickness, with subscript h denoting a homeostatic target value (Humphrey, 2008). Note, too, that the mean circumferential stress can be evaluated as $\sigma_\theta = Pa(P,C)/h(P,C)$, which emphasizes that inner radius a and wall thickness h depend on both the distending pressure P and the contractile state C of the vessel, the latter of which is influenced by flow-induced changes in endothelial-derived vasoactive molecules, including nitric oxide and endothelin-1. Hence, the vasoactive state can influence dramatically the remodeling response (Dajnowiec and Langille, 2007; Valentin et al., 2009).

Histology. Following mechanical testing, the aortas were fixed in their unloaded state in a 10% formalin solution for 24 h, stored in a 70% ethanol solution, embedded in paraffin, sectioned (5 μm thickness), mounted, and stained using three different stains: Movat's pentachrome (Mov), which stains elastin and nuclei black, collagen fibers yellowish, ground substance or glycosaminoglycans blue, and smooth muscle cells red; Verhoeff–Van Gieson (VVG), which stains elastin and nuclei black and collagen pink; and a cluster of differentiation 45 (CD45) antibody, which stains CD45-positive cells brownish-orange.

Images were acquired using an Olympus BX/51 microscope equipped with a DP70 digital camera (effective sensor resolution of 4080×3072 pixels, corresponding to a pixel size of 2.1 μm at a 2/3" (8.8×6.6 mm) sensor size) and using a 20x objective (UPlanFl 20x, NA 0.50,

optical resolution at $\lambda = 400$ nm of ~ 0.49 μm) and 0.5x tube lens, resulting in a total magnification of 10x and hence an image resolution of 0.21 μm (fulfilling the Nyquist criterion). Images were recorded using Olympus CellSens Dimension software. When arterial cross-sections exceeded the field-of-view, multiple images were acquired and stitched using Image Composite Editor software (Microsoft Research).

Three representative samples were selected for each of the four study groups, of which three sections were imaged for each of the three stains ($3 \times 4 \times 3 \times 3 = 108$ imaged sections). Custom MATLAB scripts were used to extract cross-sectional area fractions for elastin (φ^{e}), collagen (φ^{c}), smooth muscle (φ^{m}) and ground substance/glycosaminoglycans (φ^{g}). φ^{e} was averaged from VVG and Mov images; φ^{m} and φ^{g} were extracted from Mov images; φ^{c} was taken such that $\varphi^{e} + \varphi^{c} + \varphi^{m} + \varphi^{g} = 1$.

Results

Baseline Passive Mechanical Properties Are Similar Across Strains. Table 1 lists baseline data for the passive DTA for four different wild-type strains, two pure (C57BL/6J and 129SvEv) and two mixed (C57BL/6;129SvEv$_{Fbln5}$ and C57BL/6;129SvEv$_{Myh11}$). As it can be seen from the Table, there was considerable consistency in passive metrics across these four strains at individual baseline systolic pressures (measured by tail-cuff), with particular emphasis on key geometric (luminal diameter, wall thickness, and in vivo axial stretch) and mechanical (circumferential wall stress and material stiffness as well as elastic energy storage) metrics. Importantly, stored energy at systolic pressure is ~70 kPa and circumferential material stiffness linearized about this pressure is ~1.95 MPa. Indeed, the primary statistical difference across the four models was the lower energy storage and higher circumferential material stiffness in the C57BL/6;129SvEv$_{Myh11}$ strain, which was obtained by breeding *Myh11*$^{+/R247C}$ mice, noting that *Myh11*$^{R247C/R247C}$ mice have a propensity for thoracic aortopathy (Bellini et al., 2015). Nevertheless, the in vivo geometry and mechanical metrics calculated at a similar systolic blood pressure were consistent across these four strains, as would be expected of appropriate wild-type controls. Additional information supporting this conclusion can be found in Supplemental

Figures S1 and S2 and Table S1. Finally, Figure 1 compares findings specimen-to-specimen for the two pure background groups.

Baseline Contractile Properties Differ by Strain. To explore other possible similarities or differences across wild-type strains, we then focused on the C57BL/6J and 129SvEv strains, which would generally be expected to bound possible differences from the pure to mixed backgrounds. Figure 2 and Supplemental Figure S3 show vessel-level vasoactive responses during combined isobaric (fixed pressure of 90 mmHg) and axially isometric (fixed specimen-specific value of in vivo axial stretch) studies of vasoconstriction and vasodilatation. These findings are quantified in Table 2 (rows 1 and 2). As it can be seen, the percent reduction in outer diameter and associated reductions in circumferential wall stress were similar for the normotensive C57BL/6J and 129SvEv vessels when exposed to either membrane depolarization (100 mM KCl) or α_1-adrenergic stimulation (1 μM PE). Yet, vasoconstriction was dramatically different in response to the ex vivo bolus application of 1 μM AngII – there was nearly a 3-fold greater vasoconstrictive response by DTAs from the 129SvEv mice relative to the C57BL/6J mice (Figure 2 and Table 2). There was no difference in maximum endothelial function, however, which was defined as the difference in outer diameter resulting from exposure to 10 μM ACh and 1 mM L-NAME. Many other metrics of contractility are provided in Supplemental Table S2.

Responses to Induced Hypertension Differ by Strain. We then subjected C57BL/6J and 129SvEv mice to two weeks of AngII infusion at 1000 ng/kg/min. Gross examination following euthanasia and preparation for biaxial testing revealed a stable suprarenal aortic dissection in one of the C57BL/6J mice, but no dissections in the other three groups (with 129SvEv background) studied. As seen in Figure 1, there were also notable differences in the ex vivo passive behavior of the DTA despite the mean fold-increase in blood pressure being similar: 1.31-fold increase for the C57BL/6J mice (systolic pressure 167 mmHg relative to a baseline of 127 mmHg) and 1.32-fold for the 129SvEv mice (systolic pressure of 175 mmHg relative to a baseline of 133 mmHg). In particular, despite a similar reduction in the in vivo axial stretch in both strains (4%), the DTAs dilated less on average in the C57BL/6J mice (5%) than in the 129SvEv mice (13%) but thickened much more dramatically in the C57BL/6J (90%) than in the 129SvEv mice (12%). In particular, assuming similar cardiac output in normotension and AngII-

induced hypertension ($\varepsilon \sim 1$), as reported by Akishita et al. (1999), and given the similar fold-increases in blood pressure in both strains ($\gamma \sim 1.315$), one would expect for a perfect mechano-adaptation that the luminal radius would remain nearly the same ($a \rightarrow \varepsilon^{1/3} a_h = a_h$) while the wall would thicken proportional to the fold-increase in pressure ($h \rightarrow \varepsilon^{1/3} \gamma h_h = \gamma h_h$). Hence, the gross over-thickening of the DTA in the C57BL/6J mice (90% instead of the optimal 31%) can be classified as a maladaptation, which reduced values of wall stress, material stiffness, and energy storage. In contrast, the minimal thickening in the 129SvEv mice (12% instead of the optimal 32%) can be classified as an under-adaptation, which elevated values of wall stress, material stiffness, and energy storage at the new systolic pressure. For purposes of comparison, note that values of stress, stiffness, and energy storage would also increase in the case of no adaptation due solely to a "pressure-effect" on a nonlinear material. This possibility was evaluated by using the mechanical properties for the normotensive DTAs to compute the same geometrical and mechanical metrics for an acute increase in pressure to the hypertensive level but at a normal value of axial stretch (Figure 1, gray rows labeled "@ higher *P*"). As it can be seen, the predicted increases in stress, stiffness, and energy storage were only slightly higher for the 129SvEv aortas than those for the actual hypertensive values, thus suggesting a lack of adaptation or at least an under-adaptation to hypertension. In contrast, similar calculations for the C57BL/6J aortas revealed clear differences between measured and predicted values at the elevated pressure, consistent with a gross maladaptation in response to AngII-induced hypertension in this strain.

Interestingly, whereas the vasoresponsiveness of the DTAs to 100 mM KCl and 1 μM PE increased modestly in both C57BL/6J and 129SvEv mice following AngII infusion for two weeks (Table 2, Figure 2, and Supplemental Figure S3), the aforementioned greater responsiveness of the DTA in the 129SvEv mice to ex vivo exposure to 1 μM AngII largely persisted following AngII infusion in vivo. That is, the reduction in diameter and associated reduction in mean wall stress upon ex vivo stimulation of the DTA with 1 μM AngII was two-fold greater than that in the C57BL/6J mouse in the AngII-induced hypertensive mice.

Quantitative histology confirmed the over-thickening of the C57BL/6J DTA (Figure 3 and Supplemental Table S3), and localized it to both the media (increase in smooth muscle and

glycosaminoglycan area) and adventitia (increase in collagen). No significant change in medial/adventitial wall percentage was observed, confirming that the observed thickening was attributable to both layers. Immunohistochemical staining for CD45-positive ($CD45^+$) cells revealed a marked AngII-induced increase in $CD45^+$ cells in C57BL/6J DTAs, primarily in the adventitia, that was not observed in 129SvEv DTAs (Figure 4). Part of the increase observed in C57BL/6J could be explained from a lower $CD45^+$ content under normotensive conditions in this group, but absolute $CD45^+$ area increased significantly with hypertension in C57BL/6J but not in 129SvEv mice (Supplemental Table S4). On an individual level, hypertensive remodeling as quantified by wall thickness correlated with strength of contractility as well as $CD45^+$ content (Figure 5), though with contractility the strongest predictor statistically (Supplemental Table S5).

Consistent Comparisons with Prior Data. Because our methods of experimentation and data analysis have remained consistent across many aortic studies, we were able to compare the current data with previously published data from our laboratory. In particular, we have subjected C57BL/6J (Bersi et al., 2016) and C57BL/6;129SvEv$_{Fbln5}$ (Spronck et al., 2019) mice to two weeks of AngII infusion at a lower rate (490 ng/kg/min). We show absolute values in Figure 6 and fold-changes in Table 3 (each relative to its own normotensive control); the latter facilitate comparisons across the multiple groups. Note that any differences within ±5 to 7% are likely within experimental uncertainty given the different investigators and periods of study, though all were performed using the same protocols and computer-controlled devices and processed using the same custom software. In response to 1.28- to 1.38-fold increases in blood pressure over two weeks, the DTA again grossly over-thickened in the C57BL/6J mouse whereas it only thickened modestly in the mixed C57BL/6;129SvEv$_{Fbln5}$ mouse, the latter reminiscent of the aforementioned response of the DTA to a higher rate of AngII infusion in 129SvEv mice. Importantly, both the 490 and 1000 ng/kg/min rates of AngII infusion in the C57BL/6J mice yielded similar fold increases in blood pressure, $\gamma \approx 1.38$ (telemetry measurement, Bersi et al., 2016) and 1.31 (tail-cuff measurement, present study), respectively. It thus appears that the attenuated response in the C57BL/6;129SvEv aorta to AngII-induced hypertension was dominated in the lower rate of infusion by the 129SvEv ancestry. For this reason, the elevated

values of wall stress, material stiffness, and stored energy in the mixed background mice likely reflected primarily a pressure-effect, namely pressure-dependent values for an aortic wall that is otherwise similar to that in the normotensive mouse. This also holds for the decreased values in distensibility, a metric of structural stiffness commonly used clinically. To assess this pressure dependence, we again computed values of stress, stiffness, and energy storage for the normotensive groups for a hypothetical acute increase in pressure to the corresponding chronic AngII-infused value (Table 3, "@ higher *P*" rows). In this mixed background-group, we again found that the predicted fold-changes were close to the measured fold-changes in the chronically infused group, suggesting little wall remodeling in the C57BL/6;129SvEv mice. In contrast, predicted and measured fold-changes differed markedly in the C57BL/6J group, consistent with a maladaptive (over-)remodeling in these mice.

Finally, Table 3 and Figure 6 also show findings for DTAs from AngII-infused *Apoe*$^{-/-}$ mice (Bersi et al., 2017), which are on a C57BL/6 background and often used in AngII infusion studies because of their propensity toward atherosclerosis, aneurysm, or dissection. These mice were also subjected to two weeks of AngII infusion at the higher rate of infusion (1000 ng/kg/min), which can be compared directly to the data in Figure 1 for the pure C57BL/6J and 129SvEv mice. Interestingly, the *Apoe*$^{-/-}$ data reveal a greater increase in blood pressure over two weeks (γ =1.62, tail cuff), yet a remarkable near perfect geometric mechano-adaptation (inner radius dilated only 3% whereas wall thickness increased nearly 1.62-fold). The circumferential values of wall stress and material stiffness were nevertheless higher, on average, than would be expected if fully mechano-adapted. Indeed, if one looks more carefully at the time-course of changes in the AngII-infused *Apoe*$^{-/-}$ DTA in the original report (Bersi et al., 2017), results at three and then four weeks of AngII infusion again reveal a gross over-thickening of the wall, as, for example, a remarkable 3.85-fold increase for a $\gamma = 1.67$ fold increase in systolic pressure at four weeks. Hence, these results are also generally consistent with the maladaptive results observed herein for a C57BL/6 background. Note that this delayed but exuberant over-thickening was ascribed to a similarly delayed infiltration of CD45^{+} inflammatory cells, primarily in the adventitia where the fibrotic thickening occurred.

Discussion

Many studies report differences across background strains in murine (patho)biology in multiple organ systems. With regard to vascular research, it has been shown, for example, that capillary density increases more quickly in sv129 than in C57BL/6 mice following induced hind-limb ischemia (Scholz et al., 2002); that mutations to the gene that encodes the glycoprotein fibrillin-1 (*Fbn1*) and causes Marfan syndrome result in an earlier disease presentation when introduced in 129/Sv than in C57BL/6 mice (Lima et al., 2010); that consequences of elastin haploinsufficiency are greater in C57BL/6J;*Eln*$^{+/-}$x129X1/SvJ mice than in C57Bl/6J *Eln*$^{+/-}$ mice (Kozel et al., 2011); and that the atherosclerotic burden in the aortic arch, though not root, of *Apoe*$^{-/-}$ mice is greater on a 129SvEv background than on a C57BL/6J background (Tomita et al., 2012). We previously compared passive biaxial mechanical properties of the ascending aorta across seven different "wild-type" mice, including C57BL/6 and C57BL/6;129SvEv (Bellini et al., 2017b). We found few differences except in non-induced mice that were modified for tamoxifen-induction of a particular genetic target. We are not aware, however, of any prior examination of the biomechanical phenotype of the aorta across background strains in induced hypertension, including the passive and active biaxial responses that reflect structural and functional changes in hypertension.

Baseline blood pressures are higher in 129/SvJ than in C57BL/6 mice (Lum et al., 2004), which we confirmed for 129SvEv and C57BL/6J mice, though the difference was modest herein. Such differences should not be unexpected given that 129/SvJ mice have two renin genes whereas C57BL/6 mice have one (Lum et al., 2004); this difference can also be important in AngII infusion models, noting both that plasma renin tends to be lower in 129/SvJ than C57BL/6 mice and that plasma renin also tends to decrease markedly in AngII infusion (100-fold lower for 1000 ng/kg/min AngII infusion and 50-fold for 400 ng/kg/min), as one would expect of a system trying to reduce AngII levels toward normal plasma values ~$3 \cdot 10^{-10}$ mol/L (Gonzalez-Villobos et al., 2008). Whereas the luminal diameter of the DTA is similar in 129SvEv and C57BL/6J mice, the latter have a higher stroke volume and heart rate (and thus cardiac output). Yet, mean blood velocity is similar in the DTA and so too the mean wall shear stress in vivo (Tomita et al., 2012). We are the first to show quantitatively, however, that key passive

geometric and mechanical metrics are similar for the DTA for these two strains as well as for two related mixed C57BL/6;129SvEv strains (Table 1). We also found some similarities but also a key difference in the vasoconstrictive responses of the DTA between 129SvEv and C57BL/6J mice. Vasoconstriction was similar across these strains in response to phenylephrine and only slightly greater in the 129SvEv mice for KCl stimulation, but the ex vivo response to AngII was far greater in DTAs from 129SvEv than C57BL/6J mice – nearly three-fold greater in normotensive vessels and two-fold greater in hypertensive vessels. Indeed, two weeks of in vivo exposure to AngII also increased the contractile responsiveness of the DTA to KCl more in 129SvEv than in C57BL/6J mice. These differences are particularly important given the widespread usage of AngII to induce hypertension and related pathologies in mice (Berk et al., 2000; Saraff et al., 2004; Trachet et al., 2015). Similar findings have been reported for the mesenteric artery (Liu et al., 2014), which is a muscular, not elastic, artery. Specifically, Liu and colleagues showed that ring specimens from SV129 mice vasodilated less well to acetylcholine than did those from C57BL/6 mice; conversely, those from the SV129 mice contracted more strongly in response to AngII than did those from C57BL/6 mice. Because arterial remodeling is influenced strongly by vasoactivity (Dajnowiec & Langille, 2007; Valentin et al., 2009), it is important to delineate smooth muscle responses across strains, which is seldom done. For example, Hussain et al. (1999) did not detail potential differences in background in studies of the contractility of the mouse thoracic aorta from eNOS and nNOS null (on a hybrid C57BL/6;SV129 background) versus iNOS null (on a pure C57BL/6 background) mice.

The differences in hypertension-induced wall thickening between the 129SvEv and C57BL/6J mice were striking, and so too the associated consequences on wall stress, intrinsic stiffness, and energy storage. Somewhat surprisingly, the DTA did not mechano-adapt in either strain. Rather, the DTA under-adapted in the 129SvEv mice and grossly maladapted in the C57BL/6J mice, the latter consistent with prior studies in C57BL/6 mice (Wu et al., 2014; Bersi et al., 2016). Importantly, these findings suggest further that prior observations of under-adaptation of the DTA in AngII-infused C57BL/6;129SvEv mice (Spronck et al., 2019) likely arose from genetic modifiers associated with the 129SvEv strain, or more precisely from this specific sub-strain given the complex family tree of 129 mice (Simpson et al., 1997). Indeed, it would

now seem that the extreme maladaptation of the DTA in two of nine C57BL/6;129SvEv mice reported previously (Spronck et al., 2019) may have been due to a greater penetrance of the C57BL/6 versus the 129SvEv background in these two particular mice; non-uniform segregation in intercrossed mice has been reported previously (Hartner et al., 2004). Although we do not have archival tissue available to confirm our suspicion, our records indicate that these two maladaptive mice came from the same breeding pair while no other mice from that cohort descended from that particular litter. Hence, while we previously found that aging-related effects on biomechanical phenotype, especially luminal encroachment and reduction in material stiffness and elastic energy storage, are more severe than those of superimposed hypertension (Spronck et al., 2019), it now appears that effects of genetic modifiers can similarly be more important than effects of superimposed hemodynamic stress, at least when induced via chronic AngII infusion.

One cannot fail to notice in this regard that the attenuated aortic remodeling observed herein in response to in vivo AngII infusion occurred in those vessels that had a persistently increased ex vivo vasoresponsiveness to AngII. Toward that end, recall that increased wall stress is a strong stimulant for wall remodeling (Humphrey, 2008), but vasoconstriction helps to reduce pressure-induced increases in wall stress since it decreases the caliber and increases the wall thickness isochorically (cf. $\sigma_\theta = Pa(P,C)/h(P,C)$). The role of smooth muscle contraction is consistent with a recent finding in a larger cohort of C57BL/6 mice wherein a small sub-set of DTAs having modest AngII-induced hypertensive remodeling had a well preserved vasoactive capability, at least to KCl (Korneva and Humphrey, 2019). This observation is also consistent with our prior report of regional differences in AngII-induced hypertensive aortic remodeling in *Apoe*$^{-/-}$ mice wherein maladaptive fibrotic remodeling manifested in regions having a lower intrinsic vasoresponsiveness to AngII (Bersi et al., 2017). That is, only the infrarenal aorta mechano-adapted in these mice (on a C57BL/6 background) and it alone exhibits strong constrictions in response to AngII (Supplemental Figure S4). The latter is consistent with angiotensin II type 1 receptors (both subtypes a and b) existing at a higher density in the infrarenal aorta than in the suprarenal, descending thoracic, and ascending regions in C57BL/6 mice (Zhou et al., 2003; Poduri et al., 2012). Interestingly, remodeling of the aorta is similarly

modest-to-moderate in all regions in norepinephrine-induced hypertension (unpublished), noting that all regions are vasoconstrictive to phenylephrine ex vivo (Supplemental Figure S4). There is clearly a need, therefore, to investigate further the potential role of local smooth muscle responsiveness to exogenous stimuli in hypertension models, noting the often complementary roles of vasoactivity and matrix remodeling in arterial adaptations (Dajnowiec and Langille, 2007; Valentin et al., 2009). Perhaps increased vasoactivity can offset some of the distension that results from pressure loading and thereby both reduce the local wall stress and help define the mechanical state in which matrix turnover occurs.

Other factors likely play roles in vascular remodeling as well. We previously observed differential regional remodeling in a high salt + L-NAME induced hypertension in C57BL/6;129SvEv mice, again observing that the infrarenal aorta was more mechano-adaptive while the DTA was not (Spronck et al., 2019). Other potential factors of importance include sex (Ji et al., 2014), regional differences in desmin/connexin expression (Ko et al., 2001) and thus subtle differences in smooth muscle phenotype, local differences in pulsatile hemodynamic loading (Cuomo et al., 2019), and spatio-temporal differences in inflammatory burden (Wu et al., 2014; Bersi et al., 2017). As noted above, prior findings in AngII-infused *Apoe*$^{-/-}$ mice revealed a near mechano-adaptation of the DTA at two weeks of AngII infusion, but gross maladaptation thereafter (at three and four weeks of AngII infusion). Infiltration of inflammatory cells at that time (2+ weeks) appeared to contribute significantly to the exuberant collagen deposition characteristic of the maladaptation (Bersi et al., 2017). It has long been known that C57BL/6 mice have an inflammatory propensity and are particularly susceptible to diet-induced atherosclerosis, obesity, and type 2 diabetes (e.g., Paigen et al., 1985; Schreyer et al., 1998). Hence, there is similarly a need to investigate further the role of inflammatory contributors to aortic remodeling in different hypertension models, noting that inflammation is a key driver of increased central artery stiffness in humans (Park and Lakatta, 2012; Zanoli et al., 2017), which in turn increases pulse wave velocity and contributes to increases in central pulse pressure augmentation (Laurent and Boutouyrie, 2015).

Finally, there is also a pressing need to study in more detail the time-course of pressure elevation and associated aortic remodeling in both large and small vessels. Interestingly, large

(elastic) arteries tend to remodel more in response to hypertension and aging than do medium-sized (muscular) arteries, which tend to have greater contractile responsiveness. Regarding time-course, we only studied DTAs after two weeks of AngII-induced hypertension in each model, thus we do not know whether DTA remodeling might have become adaptive or maladaptive at longer times in the 129SvEv mice. We have shown previously, however, that AngII-induced hypertensive remodeling in C57BL/6 DTAs tends not to differ over two-to-four weeks of infusion (Bersi et al., 2016; Korneva and Humphrey, 2019) and that hypertension induced in C57BL/6;129SvEv mice over longer periods (13 to 18 weeks) using a high salt diet and L-NAME did not cause adverse fibrotic remodeling in the DTAs (Bellini et al., 2015; Spronck et al., 2019). Hence, again, genetic modifiers intrinsic to the 129SvEv strain appear to have a dominant role in attenuating aortic remodeling in multiple models of induced hypertension in mice.

Acknowledgments

We are grateful for our prior collaborations with Drs. Jacopo Ferruzzi, Hiromi Yanagisawa, Chiara Bellini, and Dianna M. Milewicz that yielded data for C57BL/6;129SvEv (i.e., *Fbln5*$^{+/+}$ and *Myh11*$^{+/+}$) mice (Ferruzzi et al, 2015; Bellini et al., 2015) and, so too, with Dr. David G. Harrison for data for low-rate (490 ng/kg/min) AngII infusion of C57BL/6 mice (Bersi et al., 2016), which were used herein as consistent quantitative comparators. We further acknowledge the Yale Pathology Tissue Services for histology and immunohistochemistry.

Sources of Funding

This work was supported, in part, by grants from the US NIH (R01 HL105297, U01 HL116323, P01 HL134605, U01 HL142518), from the Netherlands Organisation for Scientific Research (Rubicon 452172006), and from the European Union's Horizon 2020 research and innovation program (No 793805).

Disclosures

None.

References

Akishita M, Yamada H, Dzau VJ, Horiuchi M (1999) Increased vasoconstrictor response of the mouse lacking angiotensin II type 2 receptor. Biochem Biophys Res Comm 261:345-349.

Bellini C, Wang S, Milewicz DM, Humphrey JD (2015) $Mhy11^{R247C/R247C}$ mutations increase thoracic aortic vulnerability to intramural damage despite a general biomechanical adaptivity. J Biomech 48:113-121.

Bellini C, Bersi MR, Caulk AW, Ferruzzi J, Milewicz DM, Ramirez F, Rifkin DB, Tellides G, Yanagisawa H, Humphrey JD (2017a) Comparison of 10 murine models reveals a distinct biomechanical phenotype in thoracic aortic aneurysms. J R Soc Interface 20161036.

Bellini C, Caulk AW, Li G, Tellides G, Humphrey JD (2017b) Biomechanical phenotyping of the murine aorta: What is the best control? J Biomech Engr 139: 044501

Berk BC, Haendeler J, Sottile J (2000) Angiotensin II, atherosclerosis, and aortic aneurysms. J Clin Invest 105:1525-1526.

Bersi MR, Bellini C, Wu J, Harrison DG, Humphrey JD (2016) Excessive adventitial remodeling leads to early maladaptive aortic function in angiotensin-induced hypertension. Hypertension 67:890-896.

Bersi MR, Khosravi R, Wujciak A, Harrison DG, Humphrey JD (2017) Differential cell-matrix mechanoadaptations and inflammation drive regional propensities to aortic fibrosis, aneurysm, or dissection in hypertension. J R Soc Interface 14:20170327.

Cornel MC, Bonham VL (2017) Genomics for all in the 21st century? J Community Genet 8:249-251.

Cuomo F, Ferruzzi J, Agarwal P, Li C, Zhuang Z, Humphrey JD, Figueroa CA (2019) Sex-dependent differences in central artery hemodynamics in normal and fibulin-5 deficient mice. Proceed R Soc Lond A (in press)

Dajnowiec D, Langille BL (2007) Arterial adaptations to chronic changes in haemodynamic function: coupling vasomotor tone to structural remodeling. Clin Sci (Lond) 113: 15-23.

Davies PF (2009) Hemodynamic shear stress and the endothelium in cardiovascular physiology. Nat Clin Pract Cardiovasc Med 6:16-26.

Ferruzzi J, Bersi MR, Uman S, Yanagisawa H, Humphrey JD (2015) Decreased energy storage, not increased material stiffness, characterizes central artery dysfunction in fibulin-5 deficiency independent of sex. J Biomech Engr 137:031007.

Gleason RL, Gray SP, Wilson E, Humphrey JD (2004) A multiaxial computer-controlled organ culture and biomechanical device for mouse carotid arteries. ASME J Biomech Engr 126:787-795.

Gonzalez-Villalobos RA, Seth DM, Satou R, Horton H, Ohashi N, Miyata K, Katsurada A, Tran DV, Kobori H, Navar LG (2008) Intrarenal angiotensin II and angiotensinogen augmentation in chronic angiotensin II-infused mice. Am J Physiol Renal Physiol 295:F772-779.

Haga JH, Li YS, Chien S (2007) Molecular basis of the effects of mechanical stretch on vascular smooth muscle cells. J Biomech 40:947-960.

Hartner A, Cordasic N, Klanke G, Veelken R, Hilgers KF (2003) Strain differences in the development of hypertension and glomerular lesions induced by deosycorticosterone acetate salt in mice. Nephrol Dial Transplant 18: 1999-2004.

Hayashi K, Naiki T (2009) Adaptation and remodeling of vascular wall: biomechanical response to hypertension. J Mech Behav Biomed Mater 2: 3-19.

Huang PL, Huang Z, Mashimo H, Bloch KD, Moskowitz MA, Bevan JA, Fishman MC (1995) Hypertension in mice lacking the gene for endothelial nitric oxide synthase. Nature 377: 239-242.

Humphrey JD (2008) Mechanisms of arterial remodeling in hypertension: Coupled roles of wall shear and intramural stress. Hypertension 52: 195-200.

Humphrey JD, Tellides G (2019) Central artery stiffness and thoracic aortopathy. Am J Physiol 316: H169-182.

Hussain MB, Hobbs AJ, MacAllister RJ (1999) Autoregulation of nitric oxide-soluble guanylate cyclase-cyclic GMP signaling in mouse thoracic aorta. Br J Pharmacol 128: 1082-1088.

Ji H, Zheng W, Li X, Liu J, Wu X, Zhang MA, Umans JG, Hay M, Speth RC, Dunn SE, Sandberg K (2014) Sex-specific T-cell regulation of angiotensin II-dependent hypertension. Hypertension 64:573-582.

Ko Y-S, Coppen SR, Dupont E, Rothery S, Severs NJ (2001) Regional differentiation of desmin, connexin43, and connexin45 expression patterns in rat aortic smooth muscle cells. ATVB 21: 355-364.

Korneva A, Humphrey JD (2019) Maladaptive aortic remodeling in hypertension associates with dysfunctional smooth muscle contractility. Am J Physiol 316:H265-278.

Kozel BA, Knutsen RH, Ye L, Ciliberto CH, Broekelmann TJ, Mecham RP (2011) Genetic modifiers of cardiovascular phenotype caused by elastin haploinsufficiency act by extrinsic noncomplementation. J Biol Chem 286: 4496-4436.

Laurent S, Boutouyrie P (2015) The structural factor of hypertension: Large and small artery alterations. Circ Res 116:1007-1021.

Lee C-H, Chawla A, Urbiztondo N, Lias D, Boisvert WA, Evans RM (2003) Transcriptional regulation of atherogenic inflammation: modulation by PPARδ. Science 302: 453-457.

Lima BL, Santos EJC, Fernandes GR, et al. (2010) A new mouse model for Marfan syndrome presents phenotypic variability associated with the genetic background and overall levels of Fbn1 expression. PLoS One 5: e14136.

Liu KL, Lo M, Canaple L, Gauthier K, del Carmine P, Beylot M (2014) Vascular function of the mesenteric artery isolated from thyroid hormone receptor-α knockout mice. J Vasc Res 51: 350-359.

Lum C, Shesely EG, Potter DL, Beierwaites WH (2004) Cardiovascular and renal phenotype in mice with one or two renin genes. Hypertension 43: 79-86.

Paigen B, Morrow A, Brandon C, Mitchell D, Holmes P (1985) Variation in susceptibility to atherosclerosis among inbred strains of mice. Atherosclerosis 57: 65-73.

Park S, Lakatta EG (2012) Role of inflammation in the pathogenesis of arterial stiffness. Yonsie Med J 53:258-261.

Poduri A, Owens AP, Howatt DA, Moorleghen JJ, Balakrishnan A, Cassiss LA, Daugherty A (2012) Regional variation in aortic AT1b receptor mRNA abundance is associated with contractility but unrelated to atherosclerosis and aortic aneurysms. PLoS One 7: e48462.

Saraff K, Babamusta F, Cassis LA, Daugherty A (2003) Aortic dissection precedes formation of aneurysms and atherosclerosis in angiotensin II-infused apolipoprotein-E deficient mice. ATVB 23:1621-1626.

Schroeder F, Polzer S, Slazansky M, Man V, Skacel P (2018) Predictive capabilities of various constitutive models for arterial tissue. J Mech Behav Biomed Mater 78:369-380.

Scholz D, Ziegelhoeffer T, Helisch A, Wagner S, Friedrich C, Podzuweit T, Schaper W (2002) Contribution of arteriogenesis and angiogenesis to postocculsive hindlimb perfusion in mice. J Molc Cell Cardiol 34:775-787.

Simpson EM, Linder CC, Sargent ED, Davisson MI, Mobraaten LE, Sharp JJ (1997) Genetic variation among 129 substrains and its importance for targeted mutagenesis in mice. Nat Genet 16:19-27.

Spronck B, Ferruzzi J, Bellini C, Caulk AW, Murtada S-I, Humphrey JD (2019) Modest region-specific, sex-independent aortic remodeling when hypertension is superimposed on aging [submitted].

Tomita H, Hagaman J, Friedman MH, Maeda N (2012) Relationship between hemodynamics and atherosclerosis in aortic arches of apolipoprotein E-null mice on 129S6/SvEvTac and C57BL/6J genetic backgrounds. Atherosclerosis 220: 78-85.

Trachet B, Fraga-Silva RA, Jacquet PA, Stergiopulos N, Segers P (2015) Incidence, severity, mortality, and confounding factors for dissecting AAA detection in angiotensin II-infused mice: a meta-analysis. Cardiovasc Res 108: 159-170.

Valentin A, Cardamone L, Baek S, Humphrey JD (2009) Complementary vasoactivity and matrix remodeling in arterial adaptations to altered flow and pressure. J Roy Soc Interface 6:293-306.

Wu J, Thabet SR, Kirabo A, Trott DW, Saleh MA, Xiao L, Madhur MS, Chen W, Harrison DG (2014) Inflammation and mechanical stretch promote aortic stiffening in hypertension through activation of p38 mitogen-activated protein kinase. Circ Res 114:616-25.

Zanoli L, Boutouyrie P, Fatuzzo P, Granata A, Lentini P, Oztürk K, Cappello M, Theocharidou E, Tuttolomondo A, Pinto A, Cammà C, Licata A, Blanco J, Rastelli S, Inserra G, Castellino P,

Laurent S (2017) Inflammation and aortic stiffness: An individual participant data meta-analysis in patients with inflammatory bowel disease. J Am Heart Assoc 6:e007003.

Zhou Y, Dirksen WP, Babu GJ, Periasamy M (2003) Differential vasoconstrictions induced by angiotensin II: role of AT1 and AT2 receptors in isolated C57BL/6 mouse blood vessels. AJP 285: H2797-2803.

Highlights

- Baseline aortic geometry and properties are similar across pure (C57BL/6 and 129SvEv) and mixed (C57BL/6;129SvEv) mice, suggesting mechanical homeostatic targets;
- Aortic remodeling in response to chronic angiotensin II-induced hypertension differs dramatically between C57BL/6 and both 129SvEv and C57BL/6;129SvEv mice, suggesting a key role of genetic modifiers across different background strains;
- Maladaptive aortic remodeling in hypertensive C57BL/6 mice associates with marked increases in CD45+ cells, suggesting a key role for inflammation; and
- Modest aortic remodeling in angiotensin-induced hypertensive 129SvEv and C57BL/6;129SvEv mice associated with greater aortic vasoresponsiveness to AngII, suggesting an important role of contractility in reducing wall stress stimuli.

Figures

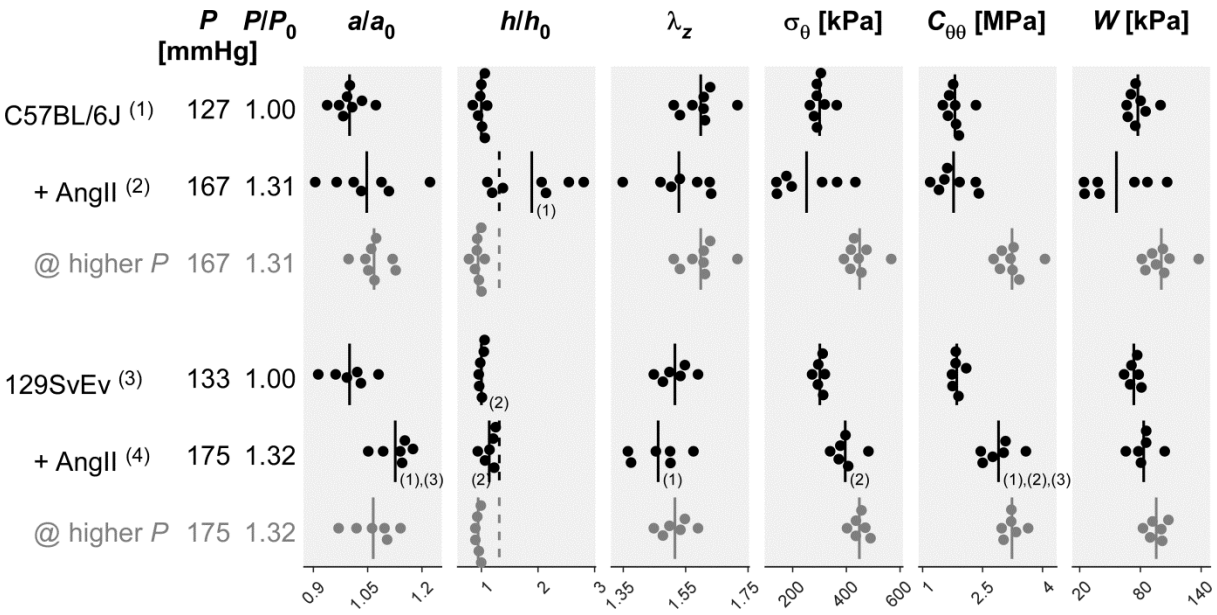

Figure 1: Passive biomechanical metrics for the descending thoracic aorta (DTA) from all four study groups (1–4; black rows): normotensive (NT) and hypertensive (HT) C57BL/6J and 129SvEv mice. Shown are group-specific systolic pressure (P), deformed inner radius (a), and deformed wall thickness (h), with original (NT) values denoted by P_0, a_0, and h_0. Also shown are the in vivo axial stretch (λ_z) as well as systolic values of circumferential Cauchy stress (σ_θ), circumferential material stiffness ($C_{\theta\theta}$), and elastically stored energy density (W). Vertical solid lines indicate arithmetic means; dashed lines in the h/h_0 column represent $\gamma = P/P_0$ and enable direct visual distinction of adaptive (lines overlap) versus under-adaptive (solid line to the left of the dashed line) or mal-adaptive (solid line to right of dashed line) remodeling. Grayed-out rows, labeled "@ higher *P*", represent predictions for NT groups evaluated at an elevated value of blood pressure that matches the AngII groups. Numbers in swarm plots indicate significant differences ($p < 0.05$) between the four groups, 1–4; no statistical tests were performed for the "@ higher *P*" rows. AngII, angiotensin II.

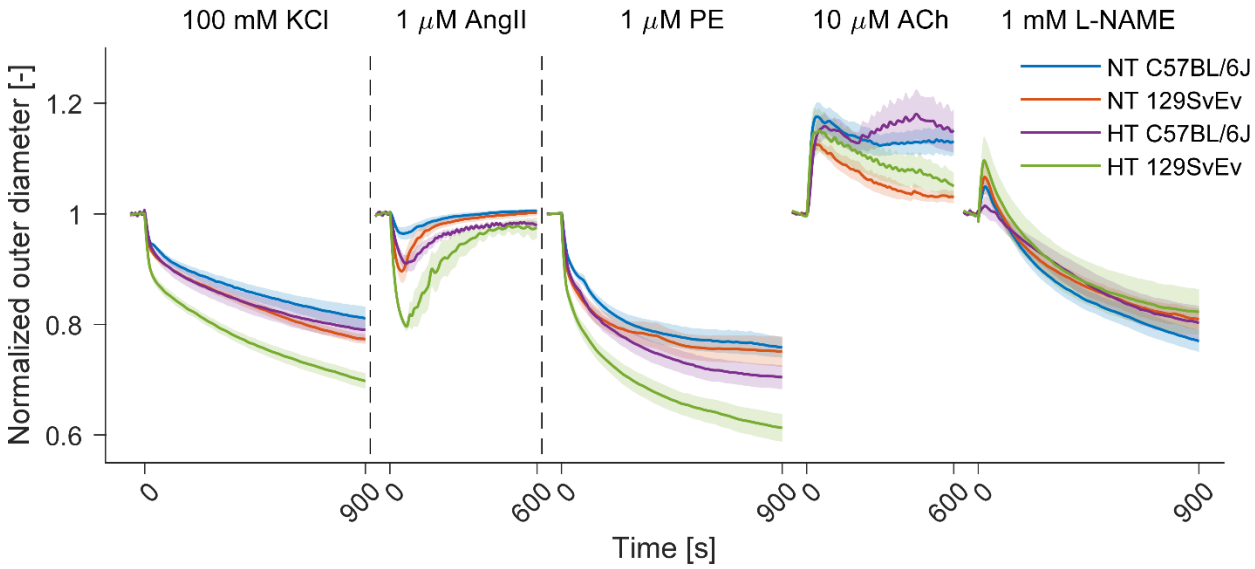

Figure 2: Aortas from 129SvEv mice show a markedly increased contraction to angiotensin II (AngII) relative to those from C57BL/6J mice, which is exacerbated after AngII-induced hypertension. Plot shows normalized outer diameter as a function of time during vasoactive testing for all four study groups: C57BL/6J and 129SvEv without and with AngII-induced hypertension (NT and HT, respectively). The thick lines indicate mean values; shaded areas indicate the standard error. Vertical dashed lines indicate 600-second washout steps. Actual outer diameter responses are in Supplemental Figure S3. PE, phenylephrine; ACh, acetylcholine; L-NAME, N_{ω}-nitro-L-arginine methyl ester.

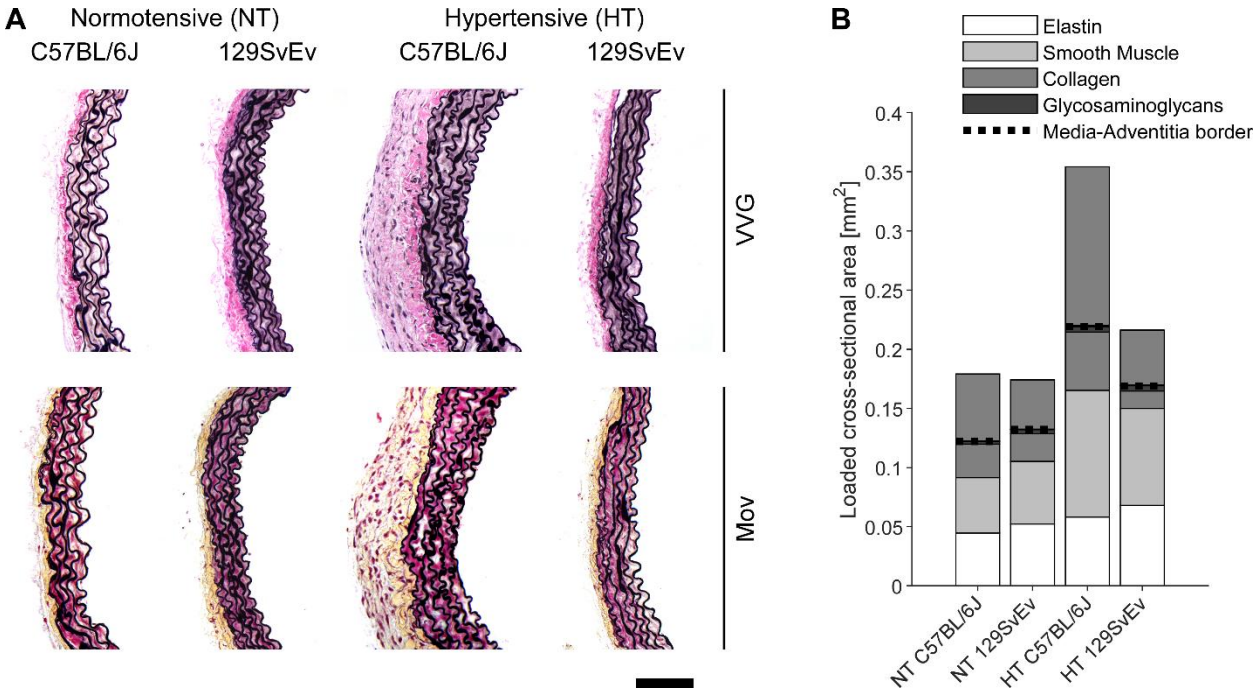

Figure 3. Angiotensin II infusion causes both medial and adventitial thickening in C57BL/6J, but not in 129SvEv mice. **A**: Representative histological sections stained using Verhoeff-Von Gieson (VVG) and Movat's (Mov) stains. Scale bar: 100 µm. **B**: Cross-sectional area of four major wall constituents for media (below dotted line) and adventitia (above dotted line).

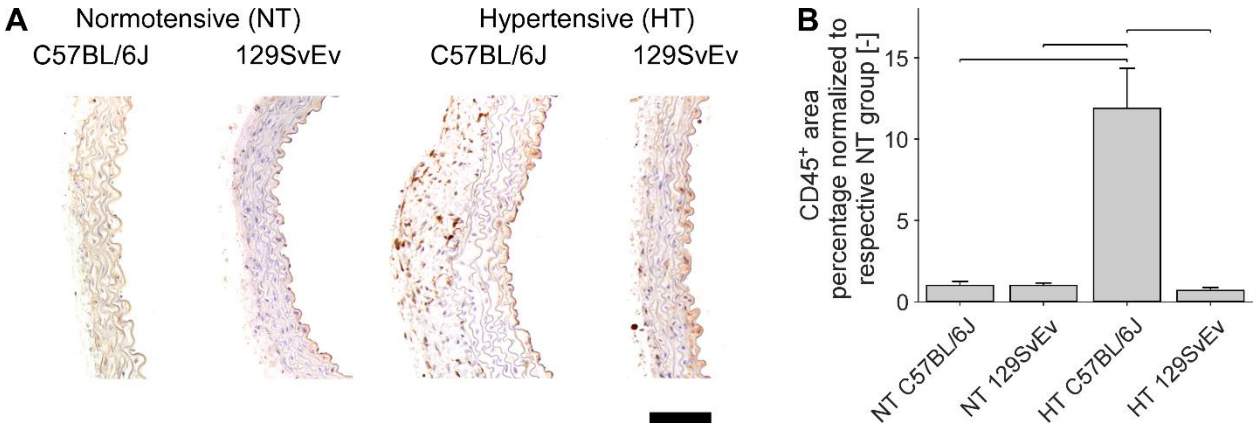

Figure 4. Aortas from C57BL/6J mice show a significant increase in cluster of differentiation 45 (CD45) expression following induced hypertension, which is not observed in 129SvEv mice. **A**: Representative immunohistochemistry sections. Scale bar: 100 µm. **B**: Normalized CD45+ cross-sectional area. Bars denote statistically significant differences (p<0.05, one-way analysis of variance with post-hoc Tukey test). NT, normotensive; HT, hypertensive.

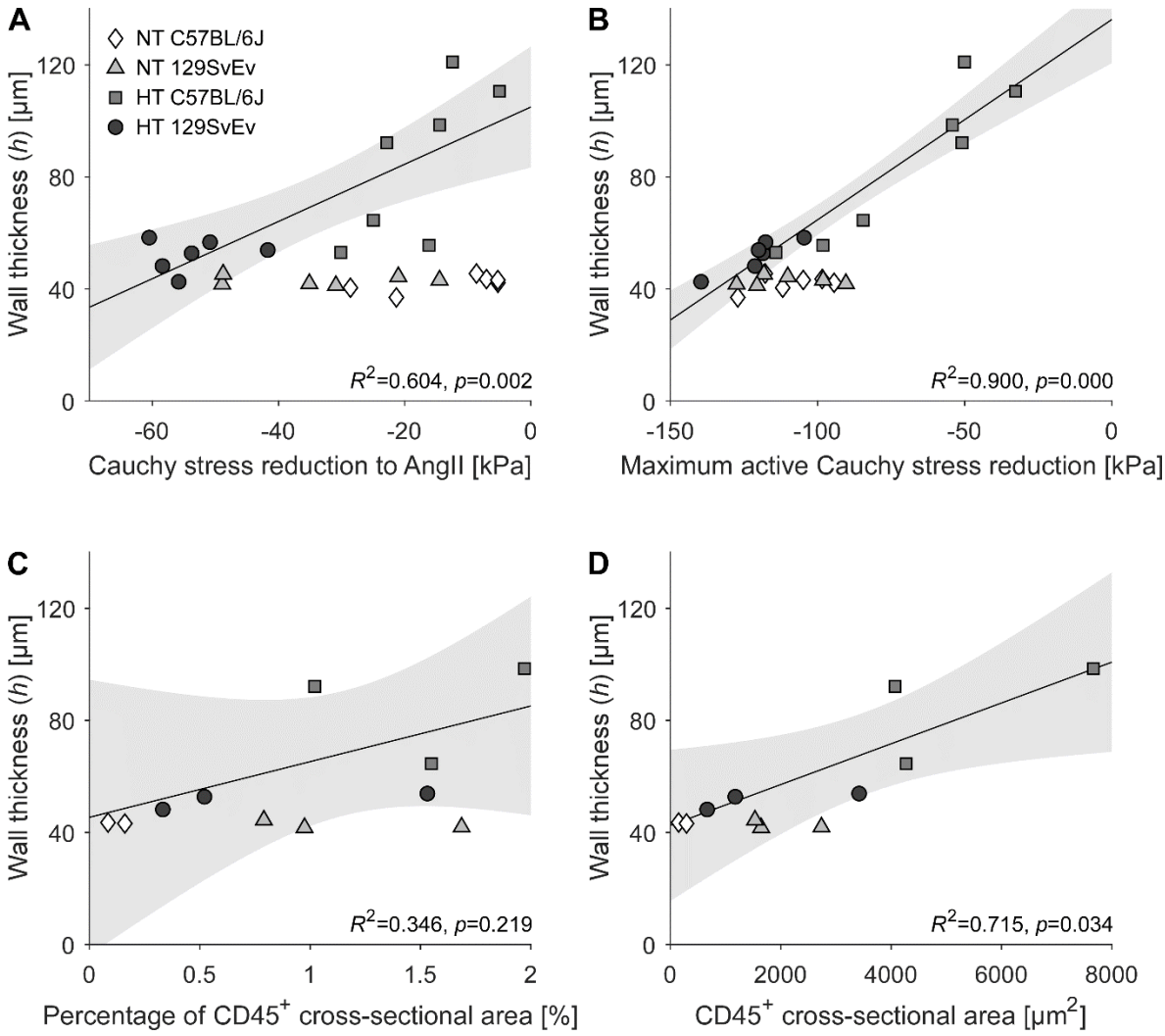

Figure 5. In hypertension, wall thickness correlates with both the ability of the smooth muscle to contract in response to angiotensin II (AngII, **A**) and other stimulants (**B**) and the presence of $CD45^+$ cells (**C** and **D**). Lines represent linear regressions on HT data only, with 95%-confidence intervals shown with grey shading. NT, normotensive; HT, hypertensive. Wall thicknesses were evaluated at a common pressure of 100 mmHg but individual-specific axial stretches.

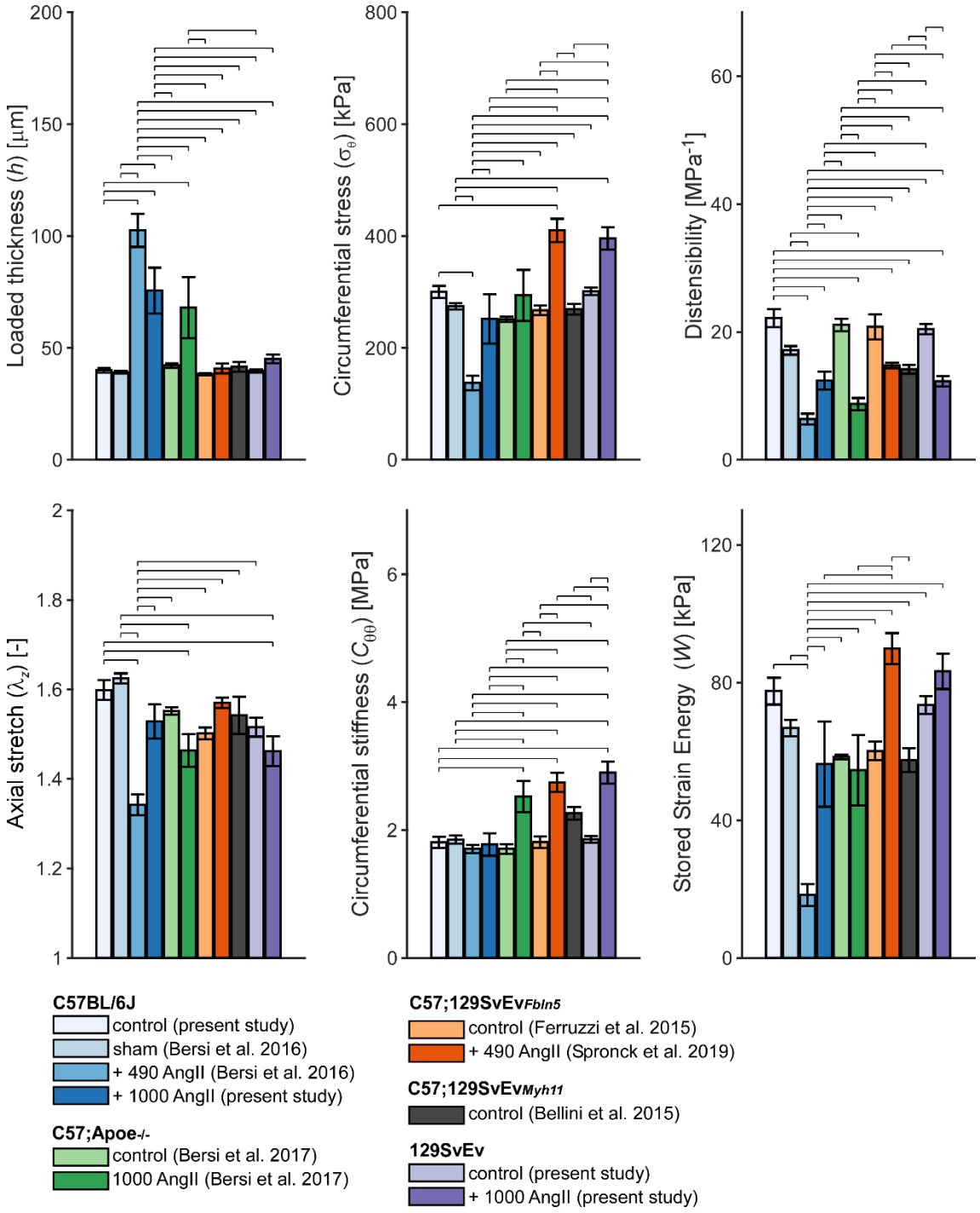

Figure 6. Effects of angiotensin II (AngII) infusion on select biomechanical metrics (mean ± standard error) across different mouse models, all for the descending thoracic aorta (DTA). AngII doses in legend are given in ng/kg/min. Bars denote statistically significant differences (p<0.05, one-way analysis of variance with post-hoc Tukey test).

Tables

Table 1. Comparison of passive biomechanical metrics for descending thoracic aortas (DTAs) of normotensive mice of four different background strains.

Mouse Model (NT)	Systolic Pressure (*P*) [mmHg]	Inner Diameter (2*a*) [μm]	Wall Thickness (*h*) [μm]	Axial Stretch Ratio (λ_z)	Circ. Stress (σ_θ) [kPa]	Circ. Stiffness ($C_{\theta\theta}$) [MPa]	Stored Energy (*W*) [kPa]
C57BL/6J (*n*=8)[(1)]	127	1410 ± 20	40.0 ± 1.1	1.60±0.02	300 ± 11	1.81±0.09	77 ± 4
C57;129SvEv$_{Fbln5}$ (*n*=5)[(2)]	120	1277 ± 28[(1)]	38.3 ± 0.4	1.50±0.01	267 ± 8	1.81±0.09	60 ± 3[(1)]
C57;129SvEv$_{Myh11}$ (*n*=5)[(3)]	124	1342 ± 38	41.5 ± 2.2	1.54±0.04	269 ± 9	2.26±0.1[(1)(2)]	57 ± 3[(1)]
129SvEv (*n*=6)[(4)]	133	1345 ± 32	39.6 ± 0.7	1.52±0.02	301 ± 7	1.85±0.05[(3)]	74 ± 3[(3)]

Mean±standard error values of systolic pressure (measured using a tail-cuff method) plus the associated inner diameter and wall thickness, in vivo value of axial wall stretch, circumferential wall stress and material stiffness, and elastically stored energy. Superscripted numbers indicate statistically significant differences across the four groups (1–4) using a one-way analysis of variance with post-hoc Tukey tests. Note the general similarity across models, consistent with that found previously for the ascending aorta (Bellini et al., 2017).

Table 2. Active vasoconstrictive (to KCl, PE, and AngII) and vasodilatory (to L-NAME and ACh) biomechanical responses of the DTA in normotensive (NT) and hypertensive (HT) mice from the two pure background strains.

Mouse Model	KCl $\%\Delta D_o$	KCl $\%\Delta\sigma_\theta$	PE $\%\Delta D_o$	PE $\%\Delta\sigma_\theta$	AngII $\%\Delta D_o$	AngII $\%\Delta\sigma_\theta$	Max EC Function $\%\Delta D_o$
NT C57BL/6J (n=6)[1]	-19 ± 2.1	-38 ± 3.9	-24 ± 1.8	-47 ± 3.2	**-4 ± 1.2**	**-8 ± 2.6**	27 ± 2.2
NT 129SvEv (n=6)[2]	-20 ± 0.9	-46 ± 1.5	-25 ± 2.8	-49 ± 4.6	**-11 ± 2.0**[1]	**-24 ± 4.1**[1]	27 ± 1.7
HT C57BL/6J (n=7)[3]	-21 ± 2.2	-48 ± 4.0	-30 ± 2.2	-64 ± 3.5[1]	**-10 ± 1.5**[1]	**-24 ± 3.5**[1]	24 ± 3.7
HT 129SvEv (n=6)[4]	-30 ± 1.4[1][2][3]	-59 ± 2.1[1][2]	-39 ± 2.5[1][2][3]	-72 ± 4.1[1][2]	**-22 ± 1.2**[1][2][3]	**-46 ± 2.5**[1][2][3]	27 ± 4.7

Mean±standard error values for vasoconstriction (100 mM KCl, 1 µM phenylephrine (PE), 1 µM angiotensin II (AngII)) induced changes (%) in outer diameter ΔD_o and mean circumferential wall stress $\Delta\sigma_\theta$ during isobaric (90 mmHg) and axially isometric (at the group-specific axial stretches, 1.49±0.03 for NT C57BL/6J, 1.45±0.04 for NT 129SvEv, 1.42±0.01 for HT C57BL/6J, and 1.41±0.04 for HT 129SvEv mice) testing. Hypertension (HT) was induced by two weeks of infusion of AngII at 1000 ng/kg/min. Shown, too, is the maximum endothelial cell (EC) function, defined by the percent difference between the outer diameter resulting from exposure to 1 mM of N_ω-nitro-L-arginine methyl ester (L-NAME) and that resulting from exposure to 10 µM of acetylcholine, with this difference normalized by the diameter associated with the acetylcholine. Superscripted numbers indicate statistically significant differences across groups (1–4) as determined by a one-way analysis of variance with post-hoc Tukey tests.

Table 3. Relative changes in passive biomechanical metrics in response to AngII-induced hypertension. All data are from previous studies using the same methods of data collection and analysis and are included for direct comparison with the present data.

	Systolic Pressure (Absolute/ Ratio)		Inner Diameter Ratio	Wall Thickness Ratio	Axial Stretch Ratio	Circ. Stress Ratio	Circ. Stiffness Ratio	Stored Energy Ratio
C57BL/6J[1]	121	1.00	1.00±0.01	1.00±0.02	1.00±0.01	1.00±0.02	1.00±0.04	1.00±0.04
+ 490 ng/kg/min AngII[2]	167	**1.38**	**0.93**±0.04	**2.62**±0.19[1]	0.83±0.01[1]	**0.50**±0.05[1]	**0.92**±0.04	**0.27**±0.05[1]
@ higher *P*	167	**1.38**	**1.07**±0.01	**0.94**±0.01	1.00±0.01	**1.57**±0.03	**1.83**±0.06	**1.32**±0.05
C57;129SvEv$_{Fbln5}$[3]	120	1.00	1.00±0.02	1.00±0.01[2]	1.00±0.01[2]	1.00±0.03[2]	1.00±0.05	1.00±0.05[2]
+ 490 ng/kg/min AngII[4]	160	**1.33**	**1.21**±0.01[1][2][3]	**1.06**±0.06[2]	1.05±0.01[2]	**1.54**±0.08[1][2][3]	**1.52**±0.08[1][2][3]	**1.50**±0.08[1][2][3]
@ higher *P*	160	**1.33**	**1.06**±0.03	**0.95**±0.01	1.00±0.01	**1.50**±0.06	**1.74**±0.09	**1.31**±0.08
C57;*Apoe*$^{-/-}$[5]	112	1.00	1.00±0.02[4]	1.00±0.03[2]	1.00±0.01[2]	1.00±0.02[2][4]	1.00±0.04[4]	1.00±0.01[2][4]
+ 1000 ng/kg/min AngII[6]	181	**1.62**	**1.03**±0.05[4]	**1.61**±0.32[2]	0.94±0.02[1][2][3][4][5]	**1.17**±0.18[2]	**1.48**±0.14[1][2][3][5]	**0.93**±0.18[2][4]
@ higher *P*	181	**1.62**	**1.10**±0.02	**0.92**±0.02	1.00±0.01	**1.93**±0.03	**2.44**±0.10	**1.52**±0.03

Mean±standard error values of systolic blood pressure plus the associated inner diameter and wall thickness, in vivo value of axial wall stretch, circumferential wall stress and material stiffness, and elastically stored energy, all as a ratio with respect to the respective normotensive groups; absolute systolic pressure [mmHg] was added for reference (first column). Presented data are from three previous studies: Bersi et al. 2016 (C57BL/6J, blood pressure measured using telemetry); and Spronck et al. 2019 (C57;129SvEv$_{Fbln5}$) and Bersi et al. 2017 (C57;*Apoe*$^{-/-}$; blood pressure measured using tail-cuff method). The C57;129SvEv$_{Fbln5}$ mice were generated by breeding *Fbln5*$^{+/-}$ mice to obtain *Fbln5*$^{+/+}$ (i.e., wild-type) mice. *n*=5 for all groups. Superscripted numbers indicate statistically significant differences (one-way analysis of variance with post-hoc Tukey tests). AngII, angiotensin II.

Supplemental Information

Genetic Background Dominates Fibrotic Aortic Remodeling During Angiotensin-Induced Hypertension in Mice

Bart Spronck[1,2], Alexander W. Caulk[1], Abhay B. Ramachandra[1], Sae-Il Murtada[1], Alexia Rojas[1], Chang-Shun He[3], Matthew R. Bersi[4], George Tellides[3,5], Jay D. Humphrey[1,5]

[1]Department of Biomedical Engineering
Yale University, New Haven, CT, USA

[2]Department of Biomedical Engineering
Maastricht University, Maastricht, The Netherlands

[3]Department of Surgery and [5]Vascular Biology and Therapeutics Program
Yale School of Medicine, New Haven, CT, USA

[4]Department of Biomedical Engineering
Vanderbilt University, Nashville, TN, USA

Address for Correspondence:

J.D. Humphrey, Ph.D.
Department of Biomedical Engineering
Yale University
55 Prospect Street
New Haven, CT 06520 USA
+1-203-432-6428
jay.humphrey@yale.edu

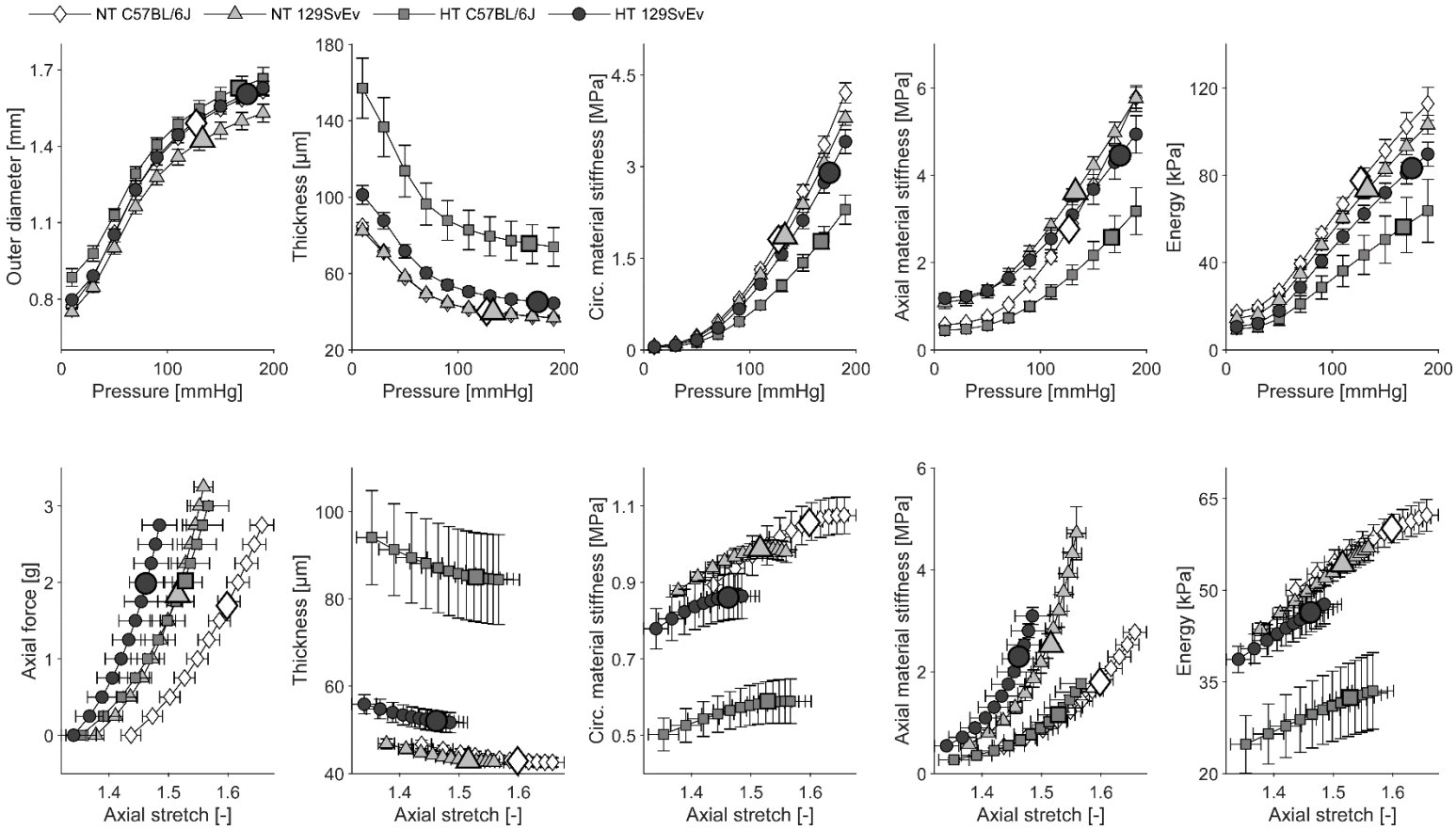

Supplemental Figure S1. Passive biomechanical metrics as a function of pressure for constant (sample-specific in vivo values of) axial stretch (top row) and as a function of axial stretch for a constant pressure of 100 mmHg (bottom row), respectively. Symbols indicate means, error bars indicate standard errors. Enlarged symbols represent values at systolic blood pressure (top row) and at in vivo axial stretch (bottom row). NT, normotensive; HT, hypertensive.

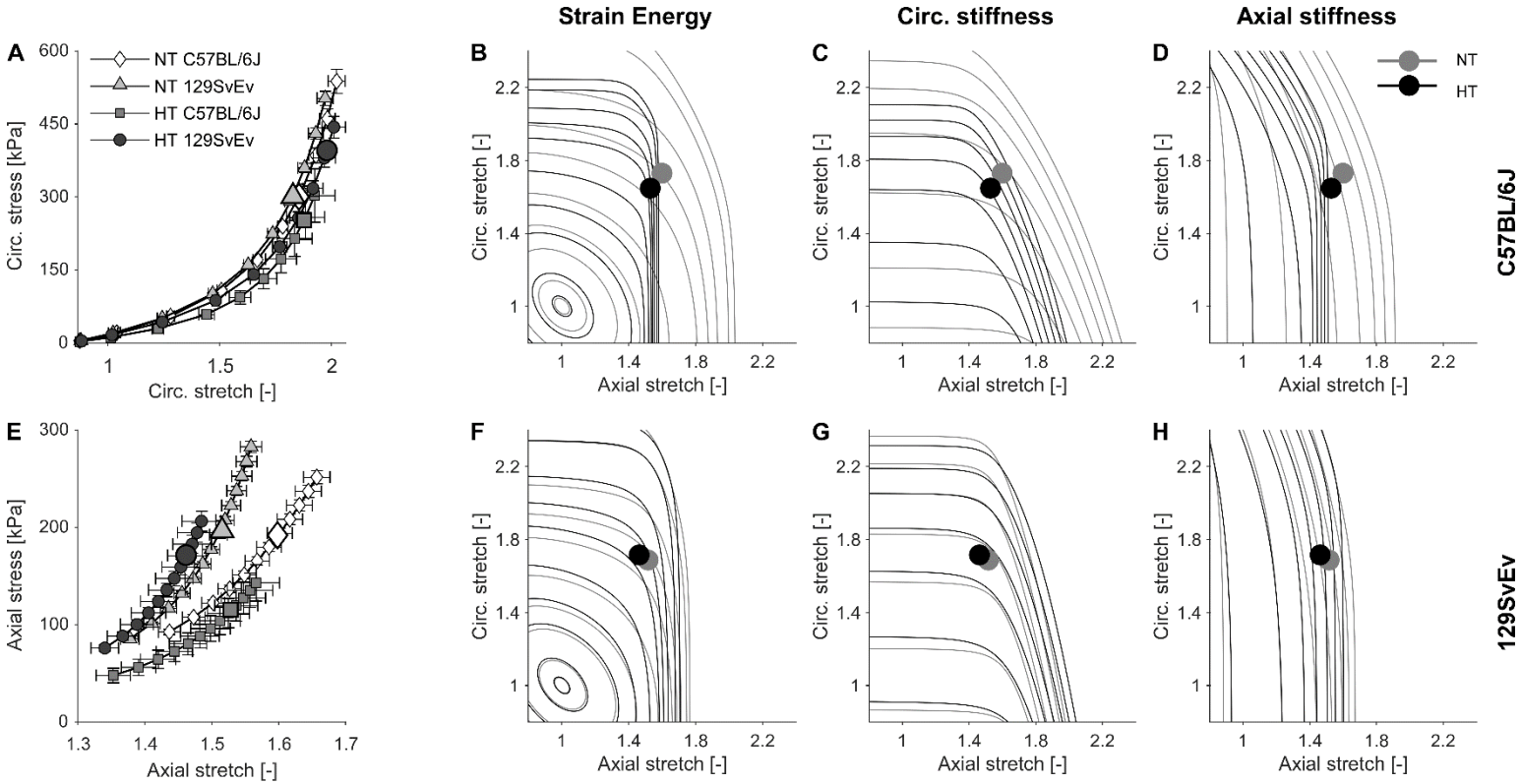

Supplemental Figure S2. Panels A and E: passive circumferential and axial stress-stretch curves, plotted at in vivo axial stretch (A) and a pressure of 100 mmHg (E). Symbols indicate means, error bars indicate standard errors. Enlarged symbols represent values at systolic blood pressure (A) and at in vivo axial stretch (E). Panels B, C, and D: group-averaged contour plots of strain energy, circumferential stiffness, and axial stiffness as a function of circumferential and axial stretch for normotensive (NT) and hypertensive (HT) C57BL/6J groups. Dots correspond to systolic blood pressure. Panels F, G, and H are the same as B, C, and D except for 129SvEv groups.

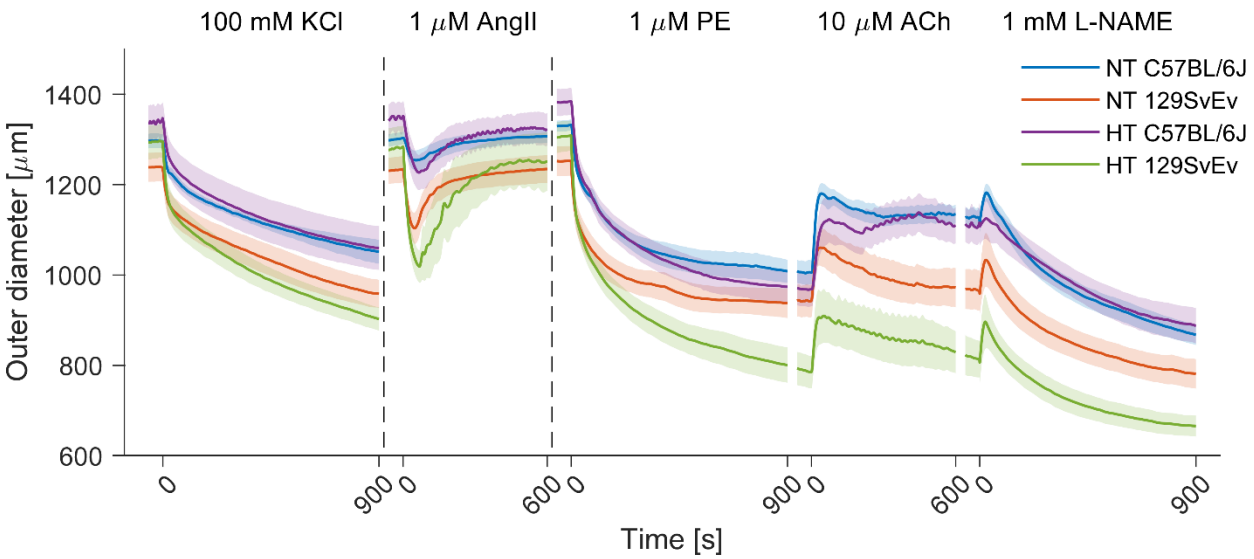

Supplemental Figure S3. Change in outer diameter (in microns) as a function of time during vasoactive testing for all four study groups: C57BL/6J and 129SvEv without and with AngII-induced hypertension (NT and HT, respectively). The thick lines indicate mean values, shaded areas indicate the standard error. Vertical dashed lines indicate 600-second washout steps. Normalized outer diameter responses are shown in Figure 2. AngII, angiotensin II; PE, phenylephrine; ACh, acetylcholine; L-NAME, N_{ω}-nitro-L-arginine methyl ester.

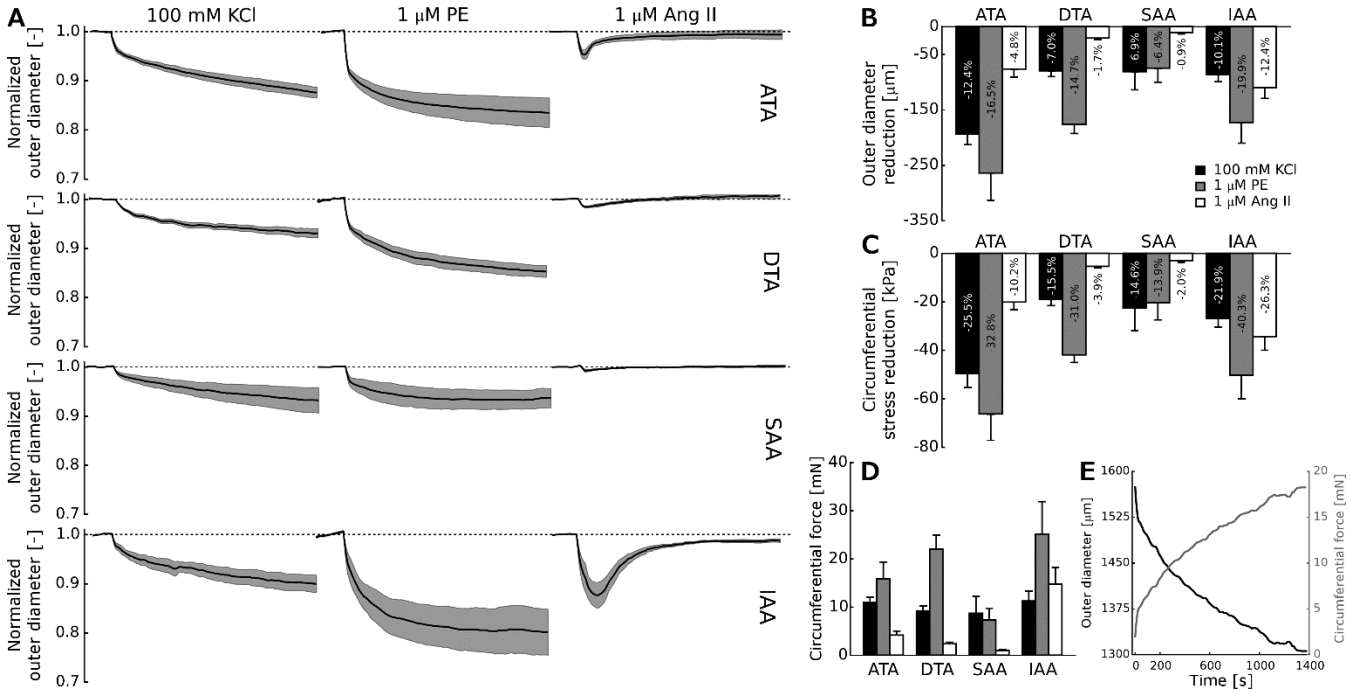

Supplemental Figure S4. (A) Time-course of induced vasoconstriction (normalized) of four regions of the aorta (ATA – ascending thoracic aorta, DTA – descending thoracic aorta, SAA – suprarenal abdominal aorta, and IAA – infrarenal abdominal aorta) from adult male *Apoe*$^{-/-}$ mice on a C57BL/6 background in response to three vasostimulants: high potassium chloride (KCl), phenylephrine (PE), and angiotensin (AngII). Note that the response to AngII is significantly greater in the IAA, a region that was previously found to mechano-adapt without fibrosis when hypertension was induced using chronic AngII infusion for 28 days (Bersi et al., 2017). Shown, too, are the mean maximal reduction in diameter (B) and circumferential wall stress (C) for the four different regions and three vasostimulants, again highlighting the more marked response of the IAA to AngII. Finally, equivalent force generation (as measured in ring myography) for the same regions and stimulants, plotted both as maximal values (D) and time-courses (E).

Supplemental Table S1: Passive biomechanical metrics for the two primary study groups (pure C57BL/6 and 129SvEv mice) subjected to normotensive (NT) or AngII-induced hypertensive (HT) conditions.

Group Number (for statistics)	**NT C57BL/6J (1)** ***n* = 8**	**NT 129SvEv (2)** ***n* = 6**	**HT C57BL/6J (3)** ***n* = 7**	**HT 129SvEv (4)** ***n* = 6**
Unloaded dimensions				
Wall Thickness, *H* [µm]	118 ± 2.1	110 ± 2.3	207 ± 16.0$^{(1)(2)}$	130 ± 4.9$^{(3)}$
Inner Diameter, 2*A* [µm]	664 ± 12	649 ± 21	625 ± 19	659 ± 15
In Vivo (Loaded) Axial Stretch, λ_z [-]	1.60 ± 0.02	1.52 ± 0.02	1.53 ± 0.04	1.46 ± 0.03$^{(1)}$
Dimensions at Diastolic Pressure *P* [mmHg]	***P* = 97**	***P* = 99**	***P* = 133**	***P* = 128**
Wall Thickness, *h* [µm]	43 ± 1.1	43 ± 0.7	79 ± 10.2$^{(1)(2)}$	48 ± 2.1$^{(3)}$
Inner Diameter, 2*a* [µm]	1296 ± 22.4	1231 ± 29.9	1397 ± 46.0$^{(2)}$	1406 ± 17.2$^{(2)}$
Dimensions at Systolic Pressure *P* [mmHg]	***P* = 127**	***P* = 133**	***P* = 167**	***P* = 175**
Wall Thickness, *h* [µm]	40 ± 1.1	40 ± 0.7	76 ± 10.2$^{(1)(2)}$	45 ± 1.9$^{(3)}$
Inner Diameter, 2*a* [µm]	1410 ± 20.2	1345 ± 31.9	1477 ± 55.3	1514 ± 24.9$^{(2)}$
Distensibility [1/MPa]	22.14 ± 1.42	20.44 ± 0.78	12.37 ± 1.41$^{(1)(2)}$	12.28 ± 0.84$^{(1)(2)}$
Additional Metrics at Systolic Pressure				
Circumferential Stretch, λ_θ [-]	1.85 ± 0.03	1.83 ± 0.03	1.88 ± 0.08	1.98 ± 0.05
Circumferential Cauchy Stress, σ_θ [kPa]	300 ± 10.8	301 ± 7.1	252 ± 44.4	396 ± 19.7$^{(3)}$
Axial Cauchy Stress, σ_z [kPa]	249 ± 12.8	250 ± 10.4	198 ± 37.4	290 ± 16.3$^{(3)}$
Circumferential Linearized Material Stiffness, $\mathscr{C}_{\theta\theta}$ [MPa]	1.81 ± 0.09	1.85 ± 0.05	1.77 ± 0.17	2.90 ± 0.17$^{(1)(2)(3)}$
Axial Linearized Material Stiffness, $\mathscr{C}_{zz}$ [MPa]	2.77 ± 0.11	3.61 ± 0.18	2.58 ± 0.40	4.45 ± 0.40$^{(1)(3)}$
Stored Strain Energy Density, *W* [kPa]	77 ± 3.9	74 ± 2.6	56 ± 12.4	83 ± 5.1
Dimensions at Fixed Pressure *P* [mmHg]	***P* = 100**	***P* = 100**	***P* = 100**	***P* = 100**
Wall Thickness, *h* [µm]	43 ± 1.1	43 ± 0.7	85 ± 10.3$^{(1)(2)}$	52 ± 2.4$^{(3)}$
Inner Diameter, 2*a* [µm]	1310 ± 22.1	1235 ± 29.9	1280 ± 35.5	1300 ± 10.7
Additional Metrics at Fixed Pressure	***P* = 100**	***P* = 100**	***P* = 100**	***P* = 100**
Circumferential Stretch, λ_θ [-]	1.73 ± 0.02	1.69 ± 0.02	1.65 ± 0.05	1.72 ± 0.03
Circumferential Cauchy Stress, σ_θ [kPa]	205 ± 6.5	192 ± 4.1	112 ± 17.0$^{(1)(2)}$	169 ± 8.8$^{(3)}$
Axial Cauchy Stress, σ_z [kPa]	192 ± 10.1	197 ± 9.8	115 ± 19.0$^{(1)(2)}$	171 ± 13.9$^{(3)}$
Circumferential Linearized Material Stiffness, $\mathscr{C}_{\theta\theta}$ [MPa]	1.06 ± 0.05	0.99 ± 0.02	0.59 ± 0.06$^{(1)(2)}$	0.86 ± 0.06$^{(3)}$
Axial Linearized Material Stiffness, $\mathscr{C}_{zz}$ [MPa]	1.79 ± 0.09	2.52 ± 0.17$^{(1)}$	1.15 ± 0.14$^{(1)(2)}$	2.29 ± 0.23$^{(3)}$
Stored Strain Energy Density, *W* [kPa]	60 ± 2.6	54 ± 2.2	32 ± 6.2$^{(1)(2)}$	46 ± 3.3

Values denote mean±standard error. Superscripted numbers in brackets indicate significant differences ($p<0.05$, one-way analysis of variance followed by Tukey's post-hoc test), and refer to group numbers.

Supplemental Table S2: Active biomechanical metrics for the two primary study groups (pure C57BL/6 and 129SvEv mice) subjected to normotensive (NT) or AngII-induced hypertensive (HT) conditions.

	Group Number (for statistics)	**NT C57BL/6J (1)** *n* = 6	**NT 129SvEv (2)** *n* = 6	**HT C57BL/6J (3)** *n* = 7	**HT 129SvEv (4)** *n* = 6
	Fixed loading and configuration				
	Axial stretch [-]	1.49 ± 0.03	1.45 ± 0.01	1.42 ± 0.04	1.41 ± 0.04
	Loaded pressure [mmHg]	90 ± 0	90 ± 0	90 ± 0	90 ± 0
	Passive outer diameter @ testing conditions [µm]	1359 ± 11	1292 ± 32	1433 ± 27(2)	1366 ± 11
100 mM KCl	**Loaded configuration**				
	Relaxed Outer Diameter [µm]	1297 ± 16.0	1239 ± 32.0	1339 ± 38.0	1295 ± 36.6
	Contracted Outer Diameter [µm]	1051 ± 26.4	958 ± 30.9	1059 ± 48.4	902 ± 25.5(1)(3)
	Change in Outer Diameter [%]	-19 ± 2.1	-23 ± 0.9	-21 ± 2.2	-30 ± 1.4(1)(2)(3)
	Stress calculations				
	Relaxed Circumferential Stretch [-]	1.62 ± 0.04	1.57 ± 0.02	1.49 ± 0.05	1.57 ± 0.06
	Contracted Circumferential Stretch [-]	1.28 ± 0.04	1.19 ± 0.01	1.12 ± 0.05(1)	1.03 ± 0.04(1)
	Relaxed Circumferential Stress [kPa]	149 ± 5.9	142 ± 3.2	75 ± 10.9(1)(2)	120 ± 6.3(3)
	Contracted Circumferential Stress [kPa]	92 ± 6.3	77 ± 2.7	39 ± 5.7(1)(2)	49 ± 3.4(1)(2)
	Change in Circumferential Stress [%]	-38 ± 3.9	-46 ± 1.5	-48 ± 4.0	-59 ± 2.1(1)(2)
	Active Circumferential Force [mN]	28 ± 3.4	30 ± 2.3	34 ± 2.7	52 ± 7.1(1)(2)(3)
1 µM AngII	**Loaded configuration**				
	Relaxed Outer Diameter [µm]	1300 ± 13.8	1232 ± 29.1	1348 ± 33.9	1280 ± 47.1
	Contracted Outer Diameter [µm]	1251 ± 23.0	1094 ± 34.8(1)	1215 ± 40.0	995 ± 42.8(1)(3)
	Change in Outer Diameter [%]	-4 ± 1.2	-11 ± 2.0(1)	-10 ± 1.5(1)	-22 ± 1.2(1)(2)(3)
	Stress calculations				
	Relaxed Circumferential Stretch [-]	1.62 ± 0.03	1.56 ± 0.02	1.51 ± 0.05	1.55 ± 0.07
	Contracted Circumferential Stretch [-]	1.56 ± 0.04	1.38 ± 0.02	1.35 ± 0.06(1)	1.19 ± 0.06(1)
	Relaxed Circumferential Stress [kPa]	150 ± 4.9	140 ± 2.5	76 ± 10.6(1)(2)	117 ± 8.7(1)(3)
	Contracted Circumferential Stress [kPa]	137 ± 4.6	107 ± 5.8(1)	58 ± 9.3(1)(2)	64 ± 7.2(1)(2)
	Change in Circumferential Stress [%]	-8 ± 2.6	-24 ± 4.1(1)	-24 ± 3.5(1)	-46 ± 2.5(1)(2)(3)
	Active Circumferential Force [mN]	5 ± 2.0	14 ± 3.0	14 ± 2.0	34 ± 4.0(1)(2)(3)
1 µM PE	**Loaded configuration**				
	Relaxed Outer Diameter [µm]	1330 ± 12.1	1252 ± 32.7	1383 ± 29.8(2)	1306 ± 33.7
	Contracted Outer Diameter [µm]	1008 ± 25.5	937 ± 32.7	974 ± 35.1	800 ± 38.9(1)(2)(3)
	Change in Outer Diameter [%]	-24 ± 1.8	-25 ± 2.8	-30 ± 2.2	-39 ± 2.5(1)(2)(3)
	Stress calculations				
	Relaxed Circumferential Stretch [-]	1.66 ± 0.03	1.59 ± 0.02	1.55 ± 0.05	1.58 ± 0.05
	Contracted Circumferential Stretch [-]	1.22 ± 0.04	1.15 ± 0.04	0.99 ± 0.05(1)	0.87 ± 0.05(1)(2)
	Relaxed Circumferential Stress [kPa]	158 ± 5.8	145 ± 2.9	83 ± 13.0(1)(2)	123 ± 7.5(3)
	Contracted Circumferential Stress [kPa]	83 ± 5.2	74 ± 6.0	30 ± 5.4(1)(2)	35 ± 7.4(1)(2)
	Change in Circumferential Stress [%]	-47 ± 3.2	-49 ± 4.6	-64 ± 3.5(1)	-72 ± 4.1(1)(2)
	Active Circumferential Force [mN]	39 ± 4.1	35 ± 5.2	56 ± 5.4	76 ± 10.1(1)(2)

Table continues on next page.

10 µM ACh / 1 mM L-NAME					
	Loaded configuration				
	Relaxed Outer Diameter w ACh [µm]	1196 ± 20.0	1073 ± 41.1	1170 ± 46.2	918 ± 62.2[(1)(3)]
	Contracted Outer Diameter w L-NAME [µm]	867 ± 22.4	780 ± 32.1	887 ± 39.0	665 ± 22.8[(1)(3)]
	Max EC activation [µm] (L-NAME od - ACh od)	329 ± 29.8	292 ± 22.9	283 ± 46.3	253 ± 61.8
	Basal EC activation [µm] (ΔL-NAME – ΔPE)	141 ± 15.3	157 ± 22.7	86 ± 20.9	135 ± 31.4
	Max SMC activation [µm] (passive - L-NAME od)	-492 ± 23.5	-512 ± 34.2	-545 ± 41.7	-706 ± 20.6[(1)(2)(3)]
	Basal SMC activation [µm] (tone - basal EC)	-170 ± 12.1	-198 ± 20.5	-136 ± 15.8	-200 ± 28.6
	Total basal tone [µm] (basal PE - passive od)	-29 ± 6.3	-41 ± 5.2	-50 ± 11.4	-65 ± 23.2
	Stress calculations				
	Relaxed Circ Stress w ACh [kPa]	123.87 ± 4.81	102.98 ± 9.30	54.60 ± 10.95[(1)(2)]	52.19 ± 9.50[(1)(2)]
	Contracted Circ Stress w L-NAME [kPa]	56.52 ± 4.53	45.30 ± 4.94	20.56 ± 3.17[(1)(2)]	17.34 ± 4.04[(1)(2)]
	Max EC activation [kPa] (L-NAME - ACh)	67 ± 5.3	58 ± 6.0	34 ± 8.4[(1)]	35 ± 9.0[(1)]
	Basal EC activation [kPa] (ΔL-NAME - ΔPE)	26 ± 2.7	29 ± 4.6	9 ± 3.1[(1)(2)]	18 ± 4.8
	Max SMC activation [kPa] (passive - L-NAME)	-109 ± 5.0	-111 ± 5.8	-69 ± 11.3[(1)(2)]	-120 ± 4.6[(3)]
	Basal SMC activation [kPa] (tone - basal EC)	-34 ± 2.1	-39 ± 4.3	-17 ± 2.9[(1)(2)]	-33 ± 6.1[(3)]
	Total basal tone [kPa] (basal PE - passive od)	-8 ± 1.8	-11 ± 1.5	-7 ± 2.0	-15 ± 5.1
	Metrics normalized to max SMC				
	Max EC diameter increase [%]	66.43 ± 3.7	59.14 ± 7.11	51.07 ± 6.14	35.22 ± 7.89[(1)]
	Basal EC diameter increase [%]	28.83 ± 3.4	31.02 ± 4.75	15.45 ± 3.24[(2)]	19.06 ± 4.34
	Basal SMC diameter decrease [%]	34.91 ± 3.0	39.32 ± 4.5	24.74 ± 1.8[(2)]	28.45 ± 4.2
	Total tone diameter decrease [%]	6.08 ± 1.4	8.30 ± 1.6	9.30 ± 2.0	9.40 ± 3.3
	Max EC circ stress increase [%]	61.75 ± 3.9	53.82 ± 7.65	46.28 ± 5.72	28.91 ± 7.43[(1)]
	Basal EC circ stress increase [%]	24.51 ± 3.2	26.02 ± 4.45	12.85 ± 2.69	14.53 ± 3.52
	Basal SMC circ stress decrease [%]	31.79 ± 2.9	36.07 ± 4.2	23.89 ± 1.4	26.53 ± 4.2
	Total tone circ stress decrease [%]	7.28 ± 1.6	10.05 ± 1.8	11.04 ± 2.3	12.00 ± 4.2

Values denote mean±standard error. Superscripted numbers in brackets indicate significant differences (p<0.05, one-way analysis of variance followed by Tukey's post-hoc test), and refer to group numbers.

Supplemental Table S3: Quantitative histology to determine elastin, smooth muscle, collagen, and glycosaminoglycan contents for the two primary study groups (pure C57BL/6 and 129SvEv mice) subjected to normotensive (NT) or AngII-induced hypertensive (HT) conditions

	Group Number (for statistics)	**NT C57BL/6J (1)**	**NT 129SvEv (2)**	**HT C57BL/6J (3)**	**HT 129SvEv (4)**
Unloaded Cross-sectional Area [mm^2]					
Media	Elastin	0.068 ± 0.002	0.079 ± 0.004	0.089 ± 0.007	0.101 ± 0.014
Media	Smooth muscle	0.073 ± 0.005	0.083 ± 0.007	0.165 ± 0.013$^{(1)(2)}$	0.122 ± 0.004$^{(1)(2)(3)}$
Media	Collagen	0.045 ± 0.006	0.036 ± 0.005	0.080 ± 0.012$^{(2)}$	0.021 ± 0.015$^{(3)}$
Media	Glycosaminoglycans	0.004 ± 0.001	0.005 ± 0.001	0.007 ± 0.001$^{(1)}$	0.007 ± 0.001
Media	Total	0.190 ± 0.011	0.204 ± 0.007	0.341 ± 0.030$^{(1)(2)}$	0.251 ± 0.003$^{(3)}$
Adventitia	Elastin	0.000 ± 0.000	0.000 ± 0.000	0.001 ± 0.000$^{(1)(2)}$	0.001 ± 0.000$^{(3)}$
Adventitia	Smooth muscle	-	-	-	-
Adventitia	Collagen	0.088 ± 0.005	0.065 ± 0.003	0.206 ± 0.035$^{(1)(2)}$	0.069 ± 0.002$^{(3)}$
Adventitia	Glycosaminoglycans	-	-	-	-
Adventitia	Total	0.089 ± 0.005	0.065 ± 0.003	0.207 ± 0.035$^{(1)(2)}$	0.070 ± 0.002$^{(3)}$
Total (both layers)		0.280 ± 0.006	0.270 ± 0.010	0.548 ± 0.025$^{(1)(2)}$	0.321 ± 0.005$^{(3)}$
Loaded Cross-sectional Area [mm^2]					
Media	Elastin	0.044 ± 0.002	0.052 ± 0.003	0.057 ± 0.005	0.069 ± 0.010
Media	Smooth muscle	0.047 ± 0.002	0.054 ± 0.004	0.106 ± 0.009$^{(1)(2)}$	0.082 ± 0.003$^{(1)(2)(3)}$
Media	Collagen	0.029 ± 0.003	0.024 ± 0.003	0.051 ± 0.008$^{(2)}$	0.014 ± 0.010$^{(3)}$
Media	Glycosaminoglycans	0.002 ± 0.000	0.004 ± 0.000	0.005 ± 0.001$^{(1)}$	0.004 ± 0.000
Media	Total	0.122 ± 0.005	0.132 ± 0.003	0.219 ± 0.020$^{(1)(2)}$	0.169 ± 0.003$^{(1)(3)}$
Adventitia	Elastin	0.000 ± 0.000	0.000 ± 0.000	0.001 ± 0.000$^{(1)(2)}$	0.000 ± 0.000$^{(3)}$
Adventitia	Smooth muscle	-	-	-	-
Adventitia	Collagen	0.057 ± 0.004	0.042 ± 0.002	0.134 ± 0.024$^{(1)(2)}$	0.047 ± 0.001$^{(3)}$
Adventitia	Glycosaminoglycans	-	-	-	-
Adventitia	Total	0.057 ± 0.004	0.042 ± 0.002	0.135 ± 0.024$^{(1)(2)}$	0.047 ± 0.001$^{(3)}$
Total (both layers)		0.179 ± 0.001	0.175 ± 0.005	0.354 ± 0.020$^{(1)(2)}$	0.216 ± 0.004$^{(3)}$
Percentage of per-layer area [%]					
Media	Elastin	36.5 ± 2.2	39.5 ± 3.0	26.5 ± 1.2$^{(2)}$	40.2 ± 5.3$^{(3)}$
Media	Smooth muscle	38.4 ± 0.6	40.1 ± 2.4	48.9 ± 1.5$^{(1)(2)}$	48.5 ± 1.2$^{(1)(2)}$
Media	Collagen	23.2 ± 2.0	17.7 ± 2.3	22.5 ± 2.3	8.7 ± 5.8$^{(3)}$
Media	Glycosaminoglycans	1.9 ± 0.2	2.7 ± 0.4	2.1 ± 0.3	2.6 ± 0.3
Adventitia	Elastin	0.5 ± 0.1	0.7 ± 0.1	0.7 ± 0.1	1.0 ± 0.1
Adventitia	Smooth muscle	-	-	-	-
Adventitia	Collagen	99.5 ± 0.1	99.3 ± 0.1	99.3 ± 0.1	99.0 ± 0.1
Adventitia	Glycosaminoglycans	-	-	-	-
Percentage of total area [%]					
Media		67.8 ± 2.5	75.8 ± 0.5	63.0 ± 5.5$^{(2)}$	78.2 ± 0.4$^{(3)}$
Adventitia		32.0 ± 2.4	24.2 ± 0.5	37.0 ± 5.5$^{(2)}$	21.8 ± 0.4$^{(3)}$

Values denote mean±standard error. Superscripted numbers in brackets indicate significant differences ($p<0.05$, one-way analysis of variance followed by Tukey's post-hoc test), and refer to group numbers.

Supplemental Table S4: Quantitative histology to determine CD45-positive area for the two primary study groups (pure C57BL/6 and 129SvEv mice) subjected to normotensive (NT) or AngII-induced hypertensive (HT) conditions

Group Number (for statistics)	**NT C57BL/6J (1)**	**NT 129SvEv (2)**	**HT C57BL/6J (3)**	**HT 129SvEv (4)**
CD45-positive area				
Unloaded [μm^2]	348 ± 91	3008 ± 413	7831 ± 1483$^{(1)(2)}$	2614 ± 708$^{(3)}$
Loaded [μm^2]	220 ± 55	1971 ± 284	5043 ± 955$^{(1)(2)}$	1754 ± 470$^{(3)}$
Percentage of total area [%]	0.123 ± 0.030	1.150 ± 0.184$^{(1)}$	1.457 ± 0.304$^{(1)}$	0.795 ± 0.208
Ratio of area percentage WRT NT [-]	1.000 ± 0.248	1.000 ± 0.160	11.884 ± 2.482$^{(1)(2)}$	0.691 ± 0.181$^{(3)}$

Values denote mean±standard error. Superscripted numbers in brackets indicate significant differences ($p<0.05$, one-way analysis of variance followed by Tukey's post-hoc test), and refer to group numbers.

Supplemental Table S5: Maximum contractility is a stronger predictor of hypertensive wall thickness than $CD45^+$ content

	Standardized β		***F*-test (model comparison)**
	coefficient	***p-value***	***p*-value**
Model #1			
Constant	-	-	
CD45+ cross-sectional area	0.846	0.034	
Model #2			
Constant	-	-	
Maximum active Cauchy stress reduction	0.972	0.001	
Model #3			
Constant	-	-	vs. #1: 0.025
CD45+ cross-sectional area	0.195	0.393	vs. #2: 0.393
Maximum active Cauchy stress reduction	0.816	0.025	

Multivariable linear regression assessment predicting wall thickness from contractility and/or CD45+ cross-sectional area. Analysis performed on hypertensive data groups only; only samples for which both contractility and $CD45^+$ histology data were available were included. Wall thicknesses were evaluated at a common, loaded pressure of 100 mmHg and at individual-specific axial stretches.